Manuscript

Click here to access/download;Manuscript;Godat_RGC_Function_Manuscript.

1 *In vivo* chromatic and spatial tuning of foveolar retinal ganglion cells in *Macaca fascicularis*

2

3 Tyler Godat*[1,2], Nicolas P. Cottaris[3], Sara Patterson[1], Kendall Kohout[1,2], Keith Parkins[1], Qiang

4 Yang[1], Jennifer M. Strazzeri[1,4], Juliette E. McGregor[1], David H. Brainard[3], William H. Merigan[1,4] &

5 David R. Williams*[1,2,4]

6 [1] Center for Visual Science, University of Rochester, Rochester, NY, United States of America.

7 [2] Institute of Optics, University of Rochester, Rochester, NY, United States of America.

8 [3] Department of Psychology, University of Pennsylvania, Philadelphia, PA, United States of

9 America.

10 [4] David & Ilene Flaum Eye Institute, University of Rochester Medical Center, Rochester, NY,

11 United States of America.

12 * Corresponding authors

13 E-mail: tgodat@ur.rochester.edu (TG), david.williams@rochester.edu (DRW)

14

15

Abstract

The primate fovea is specialized for high acuity chromatic vision, with the highest density of cone photoreceptors and a disproportionately large representation in visual cortex. The unique visual properties conferred by the fovea are conveyed to the brain by retinal ganglion cells, the somas of which lie at the margin of the foveal pit. Microelectrode recordings of these centermost retinal ganglion cells have been challenging due to the fragility of the fovea in the excised retina. Here we overcome this challenge by combining high resolution fluorescence adaptive optics ophthalmoscopy with calcium imaging to optically record functional responses of foveal retinal ganglion cells in the living eye. We use this approach to study the chromatic responses and spatial transfer functions of retinal ganglion cells using spatially uniform fields modulated in different directions in color space and monochromatic drifting gratings. We repeated these recordings in over 350 cells across three *Macaca fascicularis* primates over a time frame of weeks to months. We find that the majority of the L vs. M cone opponent cells serving the most central foveolar cones have spatial transfer functions that peak at high spatial frequencies (25-40 c/deg), reflecting strong surround inhibition that sacrifices sensitivity at low frequencies but preserves the transmission of fine detail in the retinal image. In addition, we fit to the drifting grating data a detailed model of how ganglion cell responses draw on the cone mosaic to derive receptive field properties of L vs. M cone opponent cells at the very center of the foveola. The fits are consistent with the hypothesis that midget ganglion cells are specialized to preserve information at the resolution of the cone mosaic. By characterizing the functional properties of retinal ganglion cells *in vivo* through adaptive optics, we characterize the response characteristics of these cells *in situ*.

Introduction

39

40 In primates, the fovea is a specialized region of the retina characterized by a high density of cones
41 at its center and a corresponding radial displacement of inner retinal cells and retinal vasculature.
42 These specializations, along with a vastly expanded representation in cortex [1-3], contribute to
43 the superiority of foveal vision relative to peripheral vision in spatial resolution and color
44 discrimination [1, 4-21]. To date, in excess of 20 classes of retinal ganglion cells (RGCs) have been
45 identified in macaque retina [1, 4, 6, 7, 13, 17-20, 22-52], reflecting a complex array of retinal
46 computations that precede additional processing in the brain. Despite these advances, a complete
47 understanding of these independent circuits and their role in vision and behavior remains elusive.
48 Even the precise role and scope of function of the most numerous and commonly studied RGCs,
49 the midget ganglion cells, remains controversial, and there has been relatively little study at the
50 very center of the foveola.

51

52 Electrophysiological responses from primate RGCs have been studied *in vivo* with a
53 microelectrode that penetrates the sclera [53, 54] and *in vitro* using a single microelectrode [6,
54 27] or microelectrode arrays [55, 56]. However, many recordings in primate have been made in
55 peripheral retina, often 30 to 70 degrees from the fovea because of the difficulty penetrating the
56 internal limiting membrane near the fovea. Moreover, the survival of an excised fovea is time
57 limited, and the delicate structure of the foveal pit is often strained when flattened, sometimes
58 tearing crucial circuitry. While the anatomical basis for foveal circuitry has been studied
59 extensively [7, 32, 34, 38, 57, 58] and there has been some *ex vivo* physiology of foveal RGCs, most
60 individual cell classes present in the primate fovea have not been directly studied, especially at
61 the most central locations. Retinal processing can also be inferred by recording from
62 retinorecipient neurons in the LGN, but the foveal representation of the LGN is located within a

relatively thin cell layer making such recordings challenging [59]. Moreover, it has been difficult to identify the exact foveal center *in vivo* and determining the precise retinal eccentricity of single cell recordings in LGN is difficult [5, 9, 60-62]. Furthermore, RGCs project to many different targets other than LGN, so studying these cells at the retinal level gives the best chance at providing a more complete sampling.

In this study, we use functional adaptive optics cellular imaging in the living eye (FACILE) [12, 16, 63, 64], a technique that utilizes an adaptive optics light scanning ophthalmoscope (AOSLO) to image fluorescence elicited from the activity of RGCs that express genetically encoded calcium indicators, such as those described by Chen et al [65]. Simultaneously, the cone mosaic is imaged with infrared wavelengths to map the cone density profile at the fovea. The cone mosaic images have a relatively high signal to noise ratio (SNR) and are also used to track residual eye motion in the fluorescence channel which has a relatively low SNR. Knowing the cone density profile for an individual subject allows for a more precise modeling of receptive field structure and more precise motion correction. Using this technique, we can both image and stimulate the centermost foveolar cones with spatial or chromatic stimuli and optically record the activity of the ganglion cells that are served by those cones, characterizing the physiology of the innermost foveal primate RGCs *in vivo*. Indeed, we can return repeatedly to the same ganglion cells for weeks to months, allowing repeated functional measures of the same cells. With this approach, we can use data from an individual animal that includes the optics, the cone density profile, and the RGC responses to create a detailed model of the first stages of visual processing.

Materials and Methods

87 **Animal Care**. The macaques (*Macaca fascicularis)* were housed in pairs in an AAALAC accredited
88 facility. They had free access to food and water, providing a complete and nutritious diet. To
89 supplement their ordinary lab chow, animals were given various treats daily such as nuts, raisins,
90 and a large variety of fresh fruits and vegetables. An animal behaviorist provided novel
91 enrichment items once per week, including items such as grass and treat filled bags, grapevines,
92 and forage boxes. Daily enrichment included several pieces of manipulata: mirrors, puzzle feeders
93 rotated among the animals, daily movies and/or music, as well as rotating access to a large free-
94 ranging space with swings and elevated perches during any long periods between imaging
95 sessions. All macaques were cared for by the Department of Comparative Medicine veterinary
96 staff, including four full-time veterinarians, five veterinary technicians, and an animal care staff
97 who monitored animal health and checked for signs of discomfort at least twice daily. This study
98 was carried out in strict accordance with the Association for Research in Vision and
99 Ophthalmoscopy (ARVO) Statement for the Use of Animals and the recommendations in the
100 Guide for the Care and Use of Laboratory Animals of the National Institutes of Health. The protocol
101 was approved by the University Committee on Animal Resources of the University of Rochester
102 (PHS assurance number: D16-00188(A3292-01)).
103
104 **Immune Suppression**. Two macaques (M2, M3) received subcutaneous Cyclosporine A prior to
105 intravitreal injection and imaging. Blood trough levels were collected weekly to titrate the dose
106 into a therapeutic range of 150-200 ng ml^{-1} and then maintained at that level. M2 began immune
107 suppression in March 2018 with 6 mg kg^{-1}, then stepped down a month later to 4 mg kg^{-1} which
108 was maintained until October 2019 when suppression was stopped; we believe that the cessation
109 of immune suppression was responsible for widespread apparent death of foveal ganglion cells
110 some months later in this animal (data not shown in this manuscript). M3 started immune

111 suppression in May 2019 at 6 mg kg^{-1}, then stepped down to 3.4 mg kg^{-1} which continues at time
112 of submission. M1 did not receive any immune suppression.
113
114 **AAV mediated gene delivery to retina**. Intravitreal injections were carried out in each animal as
115 previously described [66]. In M1, *7m8-SNCG-GCaMP6f* [67] was injected into the right eye; *AAV2-*
116 *CAG-GCaMP6s* was injected into the left eye of M2 and into the right eye of M3. All vectors were
117 synthesized by the University of Pennsylvania Vector Core. Before the injections, the eyes were
118 sterilized with 50% diluted Betadine, and the vector was injected into the middle of the vitreous
119 at a location approximately 4 mm behind the limbus using a tuberculin syringe and 30-gauge
120 needle. Following injection, each eye was imaged with a conventional scanning light
121 ophthalmoscope (Heidelberg Spectralis) using the 488 nm autofluorescence modality to
122 determine onset of GCaMP expression and to periodically monitor image quality and eye health.
123
124 **Anesthesia and animal preparation.** Anesthesia and animal preparation followed established lab
125 protocols as previously reported [e.g. 16, 68] and were performed by a veterinary technician
126 licensed by the State of New York (USA). All monkeys were fasted overnight prior to anesthesia
127 induction the morning of an imaging session. The animal was placed prone onto a custom
128 stereotaxic cart where it remained for the duration of the imaging session. A Bair Hugger warming
129 system was placed over the animal to maintain body temperature. Monitoring devices including
130 rectal temperature probe, blood pressure cuff, electrocardiogram leads, capnograph, and a pulse
131 oximeter, were used to track vital signs. Temperature, heart rate and rhythm, respirations and
132 end tidal CO_2, blood pressure, SPO_2, and reflexes were monitored consistently and recorded every
133 fifteen minutes. A full description of all medications used in anesthesia induction, pupil dilation,
134 intubation, and animal recovery can be found in McGregor *et. al.* [68].

135

136 **Adaptive optics imaging.** Data were collected using an AOSLO system previously described in Gray
137 et al. [63]. An 847 nm diode laser source (QPhotonics) was used as a beacon for a Shack-Hartmann
138 Wavefront Sensor (SHWS) to measure optical aberrations in each animal's eye in real time, and a
139 Deformable Mirror (ALPAO) was used to correct those aberrations in a closed loop. A 796 nm
140 superluminescent diode source (Superlum) was focused on the photoreceptor layer of the retina
141 to collect reflectance images at an approximately 2 Airy disk confocal pinhole (20 µm), with the
142 images used for both placement of stimuli and later registration (motion correction) of
143 fluorescence images. A 561 nm laser (Toptica) and three LEDs (Thorlabs, center wavelengths 420
144 nm, 530 nm, 660 nm) were used for visual stimulation of foveal cones. A 488 nm laser source
145 (Qioptiq) was focused on the ganglion cell layer to excite GCaMP fluorescence, which was
146 detected through a 520/35 nm emission filter at an approximately 2 Airy disk confocal pinhole (20
147 µm) for animals M2 and M3 and an approximately 7.5 Airy disk confocal pinhole (75 µm) for
148 animal M1, each of which was chosen to balance the tradeoff between signal strength and axial
149 resolution. It is likely that the lack of immune suppression in M1 resulted in the much poorer
150 expression of GCaMP and consequently worse SNR in that animal, which thus motivated using the
151 much larger confocal pinhole for imaging M1. The 488 nm excitation light was presented only
152 during forward scans and filled only the portion of the imaging window where ganglion cells were
153 present to avoid exposing foveal photoreceptors and biasing stimulation. The 488 nm excitation
154 light intensities on the retina were 3.4 mW cm^{-2} in M1, 3.2 mW cm^{-2} in M2, and 1.7 mW cm^{-2} in
155 M3, as presented through a dilated pupil size of approximately 6.7 mm for each animal. Retinal
156 subtenses were 780 x 570 µm in M1, 765 x 560 µm in M2, and 740 x 540 µm or 505 x 380 µm in
157 M3.

158

159 **Light safety.** The total retinal exposure to all light sources was calculated for each proposed retinal
160 location before each imaging session after measuring the optical power of each source at the
161 pupil plane (nominally 488 nm at 7-15 µW, 561 nm at 5 µW, 796 nm at 250 µW, 847 nm at 30 µW,
162 and combined 5 µW from the LEDs at 420 nm, 530 nm, and 660 nm). For all animals, the total
163 exposure was kept below the maximum permissible exposure for human retina according to the
164 2014 American National Standards Institute [69-71]. Most exposures were also kept below a
165 reduced ANSI limit that was further scaled by the squared ratio of the numerical aperture of the
166 human eye to the primate eye (~0.78) [72], though imaging sessions in M3 at the smaller FOV
167 exceeded this reduced limit. Imaging sessions were at least five days apart, so accumulated
168 exposure was not taken account into the calculations.
169
170 **Methods to maximize optical quality and signal across experiments.** Our method affords the
171 advantage of being able to record from hundreds of cells simultaneously, but there is a tradeoff.
172 The best axial resolution that can be achieved with the confocal AOSLO required for our
173 experiments is 25-30 microns, approximately the diameter of 2-3 RGC somas [27], which means
174 that in areas where the RGC layer is thick, such as the fovea [26, 46], there may be some optical
175 crosstalk from multiple cells contributing to the recorded fluorescence signal. Therefore, as part
176 of the validation of our method and to be certain in describing the physiology of individual cells,
177 we operate in two distinct modalities. The first modality is a wide imaging field of view (FOV) of
178 3.70 x 2.70 deg where we can image hundreds of RGCs across a breadth of soma locations (in M1,
179 M2 and M3), but not be certain that each cell is free of crosstalk. The second modality (only used
180 in M3) is a smaller imaging FOV of 2.54 x 1.92 deg that is centered and focused on the innermost
181 foveal slope, where the RGCs are in a monolayer—in this modality we can only image tens of cells
182 at a time, but we are certain that the signal is not contaminated by optical crosstalk. We present

183 wide field data from all three animals to show cell populations and general physiology, while we
184 present data from the smaller field only from animal M3 to draw conclusions about the physiology
185 of individual cells—the very innermost foveolar RGCs driven by the centermost cones. To ensure
186 the desired imaging FOVs were used in each experiment, the AOSLO system was calibrated using
187 Ronchi gratings of known spacing (80 lp/mm) to translate scanner control voltages into FOV
188 measurements in degrees of visual angle.
189
190 To correct for longitudinal chromatic aberration between the cone reflectance source (796 nm),
191 visual stimulus laser (561 nm), and GCaMP excitation laser (488 nm), axial source and detector
192 positions of the visible channels were optimized by initial calculation using chromatic dispersion
193 data in humans [73] scaled for the macaque eye and then further optimized empirically *in vivo*
194 using algorithms such as simplex [74] to iterate over lateral pinhole positions and find the location
195 with maximum detector mean pixel value. For the data in M3 at the inner edge of the foveal slope,
196 an additional experiment optimized the responses of 37 RGCs to 28 c/deg drifting gratings at 6 Hz
197 to find the best axial source position of the 488 nm excitation laser, to account for RGCs on the
198 foveal slope differing in axial position. Transverse chromatic aberration was not critical to stimulus
199 placement in these experiments, but lateral positions of confocal detection pinholes were also
200 optimized using similar algorithms [75].
201
202 Perhaps as a side effect of the *in vivo* viewing eye being held open for long periods of time during
203 imaging sessions, optical quality tends to degrade over the course of the experiment, slowly at
204 first, but more quickly after the first hour of imaging. To mitigate this, all grating stimuli were
205 presented at the beginning of a session when optical quality was the highest, and only for the first
206 30 minutes, to minimize degradation of high spatial frequency responses.

207

208 Lastly, the isoplanatic patch size of our system is approximately 1-1.5 deg, which is smaller than
209 both of the imaging fields (3.70 x 2.70 deg and 2.54 x 1.92 deg) used in this study. This degrades
210 quality across the entire image and produces field aberrations towards the edges of the images
211 where some ganglion cells were imaged or cones were stimulated. This anisoplanatism, coupled
212 with the fact that the wavefront correction is at a different wavelength than stimulation, means
213 that there could be defocus (see Modeling section) or higher order residual aberrations that
214 preferentially blur high spatial frequency gratings. Care was taken to mitigate or optimize these
215 sources of residual blur, but they cannot completely be eliminated with our current instrument.
216 Therefore, the spatial frequency responses we measured represent a lower bound for the cell
217 responses *in situ* when all sources of residual blur are removed.

218

219 **Chromatic Stimuli**. To drive the chromatic responses of RGCs connected to foveal photoreceptors,
220 we presented a 1.3 deg diameter spatially uniform, circular LED stimulus (Thorlabs, center
221 wavelengths 420nm, 530nm, 660nm) through a Maxwellian view system [76]. The stimulus was
222 sinusoidally modulated in time. Mean intensities on the retina and temporal frequencies were 6.8
223 mW cm^{-2} at 0.2 Hz in M1, 7.0 mW cm^{-2} at 0.2 Hz in M2, and 7.6 mW cm^{-2} at 0.15 Hz in M3. The
224 slow temporal frequencies were chosen to accommodate the slow temporal response of the
225 GCaMP6 calcium indicator [65] and were adjusted by 0.05 Hz in M3 to avoid potential confound
226 with the respiration rate in that animal. The LED primary wavelengths were chosen to maximize
227 excitation of the L, M, and S cone photopigments [77] while minimizing significant confound by
228 macular pigment absorption [78, 79], the spatial distribution of which was not measured in this
229 study. Each stimulus presentation was 90 s long, following a 30 s adaptation period in which the
230 mean luminance white point and excitation laser were on. The cone fundamentals were

231 constructed using the Govardovskii standard template [80, 81] and the wavelengths of peak
232 absorption for macaque primates [82]. The transmissivity of the eye (including cornea, aqueous,
233 lens, and vitreous) was modeled using measured data from the rhesus macaque [83]. To generate
234 the luminous efficiency function, an equal weighting of the L and M cone fundamentals was used,
235 as the ratio of L and M cones in macaques is close to unity on average [84]. The LEDs were
236 calibrated using a spectrometer (Ocean Optics) validated by a NIST traceable blackbody source.
237 Five silent substitution [85] stimuli were presented at the foveal center while GCaMP responses
238 were recorded. The Psychophysics Toolbox [86] for MATLAB was used to calculate the appropriate
239 power modulations needed: a nominally isoluminant stimulus targeting both L and M cones in
240 counterphase (L modulation 15%, M modulation 17%), an L cone isolating stimulus (24%
241 modulation), an M cone isolating stimulus (33% modulation), an S cone isolating stimulus (92%
242 modulation), and an achromatic luminance stimulus (100% modulation, all cone classes). There
243 was also a control stimulus where the adaptation period was followed by continued presentation
244 of the mean luminance white point. Within one imaging session, each of the stimuli used in that
245 session was presented three times and responses were averaged within the experiment. In M1,
246 only one experiment was performed. In M2 and M3, two experiments across the entire width of
247 soma locations (large imaging FOV) were performed and responses across sessions were
248 averaged. In M3, three separate experiments at the innermost foveal RGCs (small imaging FOV)
249 were performed and averaged.
250
251 **Grating Stimuli.** To probe the spatial configuration of foveal RGC receptive fields, we presented
252 monochromatic (561 nm) horizontally-oriented sinusoidal drifting gratings at 6 Hz and 100%
253 contrast. The grating stimuli were presented within the scanned imaging FOV and occupied a
254 square subregion that was either 1.9 deg (large imaging FOV) or 1.3 deg (small imaging FOV) in

255 extent. Mean light intensities on the retina were 1.72 mW cm^{-2} in M2 (large imaging FOV), 1.8 mW
256 cm^{-2} in M3 (large imaging FOV), and 3.2 mW cm^{-2} in M3 (small imaging FOV) imaging only the
257 innermost RGCs closest to the center of the foveola. No data from drifting gratings is shown for
258 animal M1, as the signal was too weak and noisy to produce reliable data from these stimuli. The
259 temporal frequency of these gratings was too fast to allow GCaMP6 to track modulation, so
260 cellular responses were characterized by quantifying the increase in steady fluorescence during
261 stimulation, as opposed to using fluorescence modulation as was done for the slower chromatic
262 stimuli. Grating stimuli were 45 s in duration and were preceded by 15 s adaptation to both the
263 mean luminance of the 561 nm stimulus laser and the 488 nm imaging laser.
264
265 In the small imaging FOV used with M3, the increased resolution meant that the spatial frequency
266 range was 4 c/deg to 49 c/deg. A control and 14 gratings were presented twice each within a
267 session and responses were averaged. Gratings were presented in decreasing order of spatial
268 frequency, to minimize reduction in high spatial frequency response related to decreasing optical
269 quality over the course of the experiment. There were three sessions at the small FOV in M3, and
270 the variability and averages are shown in the results. We note that as gratings were only
271 presented in one orientation, the responses of some cells might be modified by orientation
272 selective effects [87].
273
274 In M2 and M3 at the large imaging FOV, a control (spatially uniform mean luminance) and 14
275 gratings varying in spatial frequency from 2 c/deg to 34 c/deg were presented. Each grating was
276 presented twice within a session and responses were averaged for one session in M2 and across
277 two sessions in M3. These data are not presented in the results because they did not include high

278 enough spatial frequency responses that permit the modeling used in this work (see Supplement
279 **S2 Fig.**).
280
281 **Data analysis**. To remove blurring and other effects of residual eye movements present in the raw
282 recordings, each video frame of the fluorescence recording was co-registered using corresponding
283 frames from a high signal-to-noise reflectance video of the photoreceptor layer at the same
284 retinal location. During imaging, a reference frame was taken in the reflectance channel to allow
285 for real-time stabilization; this reference frame was also used as the reference for the frame-to-
286 frame cross-correlation method image registration [88] of all videos taken at that location. One
287 registered video, typically one of the videos corresponding to the peak spatial frequency response
288 (usually 10 – 30 cycles/deg), was temporally summed to create a high SNR fluorescence image of
289 the ganglion cell layer, and individual ganglion cells were segmented using the open-source
290 software GIMP. Typically, all identifiable cells in the focal plane were segmented, though cells
291 were excluded if the boundaries between two or more adjacent cells were unclear. The
292 segmentation mask from GIMP was exported to MATLAB, where it was applied to all registered
293 videos at that location to isolate data from individual RGCs. For every frame, the mean of the
294 signal within each cell mask was computed to produce an average signal time course for each cell.
295 When the same stimuli were repeated across multiple sessions, the signal time courses for each
296 cell were averaged across all sessions.
297
298 For the chromatic data, the temporal speed of the flicker (0.15-0.20 Hz) was well within the
299 temporal resolution of the GCaMP6, thus cells responding to the stimulus exhibited a quasi-
300 sinusoidal modulation in fluorescence level where the amplitude and phase depended on the
301 receptive field properties of the cell and the frequency of the response depended on the stimulus

302 frequency. Each cell's time course was filtered using a Hann windowing function before being
303 Fourier transformed into the frequency domain. The Fourier amplitudes were normalized by
304 subtracting the mean noise at higher frequencies (0.32 Hz - 1.08 Hz) and then dividing by the
305 standard deviation of the noise to produce a response metric equivalent to the sensitivity index
306 d'. The metric was computed for each stimulus for every cell, so that the cells could be plotted in
307 two different configurations from the literature [e.g. 60]. In animals M1 and M2, where an L-M
308 nominally isoluminant stimulus, an S-isolating stimulus, and an achromatic/luminance stimulus
309 were used, no further analysis was needed, and the data was simply plotted along S vs. L-M axes.
310 In animal M3, since single cone isolating stimuli were used for L, M, and S cones, it was possible
311 to reproduce cone weighting plots such as those in Derrington *et. al.* [60]. As in that paper, we
312 calculated the cone weights by dividing the response metric by the cone modulation from the
313 stimuli and normalized them all such that the sum of all cone weights added to unity.
314
315 For the spatial frequency data, the temporal speed of the drifting gratings (6 Hz) exceeded the
316 temporal resolution of the GCaMP6s indicator [65], thus cells responding to the grating exhibited
317 an overall increase in fluorescence that plateaued after approximately 10-20 s. The background
318 level for each cell was calculated as the mean of the first 10 s of fluorescence during the
319 adaptation period, while the signal was calculated as the mean of the last 10 s of fluorescence
320 recorded during the presentation of the stimulus. The ΔF/F metric commonly used in calcium
321 imaging was calculated for each spatial frequency as the background response at that frequency
322 subtracted from the signal at that frequency, all divided by the signal at 17 c/deg, a spatial
323 frequency producing a robust response across the majority of the cells. This function of ΔF/F with
324 respect to spatial frequency is what we refer to as a spatial transfer function (STF) for each RGC
325 measured. An error metric was also calculated for each ΔF/F measurement by using the partial

326 differential error propagation formula using variances [89] and the measured variances in the
327 background response, the signal response, and the signal at 17 c/deg.
328
329 **Modeling of photoreceptor mosaic and RGC response characteristics**. To connect the measured
330 spatial transfer functions (STFs) to the receptive field (RF) organization of the underlying RGCs,
331 we employed a computational model that simulates optical, spectral, spatial, and temporal
332 components of the AOSLO stimulation apparatus, as well as the animal's optics and cone mosaic
333 structure. The model computed cone mosaic responses to simulations of the stimuli used to
334 measure the STF and derived an STF model fit for the RGC under study. The model assumed that
335 cone signals are pooled linearly and instantaneously (ignoring temporal pooling dynamics) by
336 center and surround mechanisms of an RGC according to a difference of Gaussians (DoG) [90]
337 spatial profile. The parameters of the DoG (and therefore the cone pooling weights) were
338 estimated by minimizing the error between the model STF and the measured *in vivo* fluorescence-
339 based STF. A model scenario where the center mechanism's Gaussian weighting was replaced by
340 center weighting on just a single cone was also considered. The modeling pipeline, depicted
341 schematically in Figure 6, was implemented within the Imaging Systems Engineering Tools for
342 Biology (ISETBio) software framework [91, 92].
343
344 The drifting monochromatic sinusoidal gratings (Fig 6a) used to measure RGC STFs via the AOSLO
345 apparatus (Fig 6b) were modeled as temporal sequences of ISETBio spatial-spectral radiance
346 scenes, where each scene models one frame of the displayed stimulus. The spectral
347 characteristics, spatial extent, and the temporal properties of the AOSLO display subsystem were
348 taken into account in generating the ISETBio scenes. The spectral profile of the monochromatic
349 beam was modeled as Gaussian shaped with a peak at 561 nm and a full-width-half-max (FWHM)

350 of 5 nm with a mean irradiance on the retina of 1.29 mW cm^{-2}. The power estimate included
351 absorption by the lens pigment. The visual stimulus as imaged on the retina had a pixel size of
352 1.03 µm (0.005 deg) with spatial extent 140 x 140 µm (0.7 x 0.7 deg). All sinusoidal gratings were
353 modeled with a nominal contrast of 1.0, drifting at 6 Hz with a refresh rate of 25.3 Hz for a duration
354 of 666 ms (4 cycles).
355
356 The animal's optics during AOSLO-based stimulation were modeled as a diffraction-limited optical
357 system (Fig. 6c) with a small amount of residual defocus blur (Fig. 6d). The diffraction limit was
358 obtained using the 6.7 mm pupil diameter employed in the experiment, assuming a conversion
359 between degrees of visual angle and retinal extent of 199 µm/deg. Residual blur in the AOSLO,
360 which might occur due to a slight defocus of the stimulus with respect to the plane of cone inner
361 segments in the retina, was modeled by adjusting the Zernike defocus coefficient used to compute
362 the optical point spread function. Residual blur could also be generated by any off-axis aberrations
363 in the system, imperfect AO correction, or other sources, so the Zernike defocus coefficient was
364 used as a proxy for all sources of residual blur. The amount of residual blur was not known *a priori*
365 and was estimated as part of model fitting as described below. The temporal sequence of ISETBio
366 spatial-spectral radiance scenes that model the AOSLO stimulus were passed via the simulated
367 optical system to generate a corresponding sequence of spatial-spectral retinal irradiance images,
368 which were processed by the cone mosaic model as described next.
369
370 An ISETBio model of the animal's cone mosaic (Fig. 6e) was generated from cone density maps
371 measured during AOSLO imaging, using an iterative algorithm described previously [91]. The
372 spatial extent of the modeled cone mosaic was 1.3 x 1.3 deg, with a maximal cone density of
373 270,200 cones mm^{-2} with relative L:M:S cone densities of 0.48:0.48:0.04 (quasi-regular S cone

packing, random L and M cone packing), and without a tritanopic (S-cone free) area at the fovea. Cones were modeled with Gaussian entrance apertures with a characteristic radius equal to $0.204 * \sqrt{2} * D$, where *D* is the inner segment diameter measured during AOSLO imaging [10]. In this cone mosaic model, cone outer segment lengths and macular pigment all varied with eccentricity [91], and the cone quantal efficiencies were based on the Stockman-Sharpe (2000) normalized absorbance measurements [93, 94]. The modeled macular pigment density is taken as the human values provided by Stockman *et. al.* (1999) [93] (http://www.cvrl.org/database/text/maclens/macss.htm), and the modeled lens pigment density is for young human subjects (< 20 years) as reported by Pokorny *et. al.* [95].

To compute a cone's excitation, the spatial-spectral irradiance impinging on the retina was first spectrally weighted by the product of macular pigment transmittance and by each cone's spectral quantal efficiency, subsequently integrated over wavelength, and spatially integrated over the cone's Gaussian aperture. This excitation response was integrated over the temporal duration of each stimulus frame (39.5 ms), to estimate a spatial map of the expected excitation events count $E^j(\omega,t)$, for the *j*-th cone in the mosaic, at time *t*, in response to a drifting grating of spatial frequency ω (Fig 6f). In these simulations, we did not include Poisson noise in $E^j(\omega,t)$, nor did we introduce positional jitter between the cone mosaic and the retinal stimulus due to fixational eye movements. In the measured AOSLO data, the animals were anesthetized with eye muscles paralyzed, and digital tracking was employed for stimuli, so retinal motion relative to stimuli was minimized.

Assuming that cones are adapted to the mean background irradiance, the spatiotemporal excitation response $E^j(\omega,t)$ was converted to a spatiotemporal modulation response, $R^j(\omega,t)$, (Fig

6g) by first subtracting the excitation of the cone to the background stimulus E_0^j, and then dividing by it separately for each cone *j,* i.e.:

$$R^j(\omega,t) = \frac{E^j(\omega,t) - E_0^j}{E_0^j}$$

This operation captures in broad strokes an important effect of the photocurrent generation process which converts cone absorption events in the inner segment into ionic currents flowing through the cone outer segment, and which in effect down-regulates the stimulus-induced cone excitation rate with respect to the background cone excitation rate.

Model ganglion cell responses $RGC(\omega,t)$, were computed from the cone contrast responses by weighting responses with corresponding center and surround cone weights (Fig 6h), followed by spatial pooling within the antagonistic center and surround mechanisms (Fig. 6i) as follows:

$$\begin{aligned} RGC(\omega,t) &= RGC_c(\omega,t) - RGC_s(\omega,t) \\ &= \sum_j W_c^j * R^j(\omega,t) - \sum_j W_s^j * R^j(\omega,t) \end{aligned}$$

where W_c^j and W_s^j are the weights with which the center and surround mechanisms respectively pool the responses $R^j(\omega,t)$. We did not model temporal filtering or delay between center and surround responses. Although real RGC responses may be affected by both temporal filtering and a center-surround delay, measurements in this study only recorded the amplitude of responses at one temporal frequency with no response phase information, so we could not meaningfully estimate temporal RGC parameters.

To make computation of cone weights more tractable, we assumed that the spatial distribution of cone weights to the center and surround mechanisms had concentric, radially-symmetric

Gaussian profiles (multi-cone RF center scenario), or that the center drew on a single cone with a Gaussian surround (single-cone RF center scenario):

$$W_c^j = \begin{cases} k_c * \exp\left[-\left(\frac{d_j}{r_c}\right)^2\right] & (multi - cone\ RF\ center\ scenario) \\ k_c & (single - cone\ RF\ center\ scenario) \end{cases}$$

$$W_s^j = k_s * \exp\left[-\left(\frac{d_j}{r_s}\right)^2\right]$$

where d_j is the distance between cone-j and the spatial position of the center mechanism of the model RGC (which is taken as the geometric centroid of the locations of the cones driving the center mechanism). The parameters k_c, k_s, r_c, and r_s, which represent the center and surround peak sensitivities and characteristic radii, respectively, of the DoG RF model (Fig. 6 l,m) were determined by minimizing the root mean squared error (RMSE) between the model-predicted STF, $STF^m(\omega)$, and the measured STF, $STF^{\Delta F/F}(\omega)$, (Fig. 6k) accumulated over all spatial frequencies ω:

$$RMSE = \sqrt{\frac{1}{N} * \sum_{\omega=\omega_1}^{\omega_n} \frac{\beta(\omega)}{\epsilon(\omega)} * [STF^m(\omega) - STF^{\Delta F/F}(\omega)]^2}$$

where $\epsilon(\omega)$ is the standard error of the mean of the $STF^{\Delta F/F}(\omega)$ measurement, and $\beta(\omega)$ is a high-spatial frequency boost factor which linearly increases with spatial frequency from 0.1 to 1.0 over the spatial frequency range 4.7 to 49 c/deg. This boost factor was introduced to emphasize high spatial frequency measurements, the stimulus regime which is maximally informative about the properties of the center mechanism.

In some cells, and for certain recording sessions, the measured $STF^{\Delta F/F}(\omega)$ dropped below zero for the lowest spatial frequencies. When this occurred, it was accompanied by an apparent overall

downward shift in $STF^{\Delta F/F}(\omega)$ across all frequencies, so we assumed that in such cases the background fluorescence was overestimated. To compensate for this, we fit the model to $STF^{\Delta F/F}(\omega) - \min(STF^{\Delta F/F}(\omega))$ instead of $STF^{\Delta F/F}(\omega)$ in cases where $STF^{\Delta F/F}(\omega)$ dropped below zero for any spatial frequency.

To reduce the chance of the minimization algorithm getting stuck at a local minimum of the error function, we employed a multi-start minimizer which was run 512 times, keeping the results from the starting point with the minimum RMSE.

The model-predicted STF, $STF^{m}(\omega)$, was computed by fitting a sinusoidal function to $RGC^{m}(\omega, t)$,

$$A(\omega) * \sin[2\pi f t - \theta]$$

where f is set to the temporal frequency of the drifting gratings, and θ, A(ω) are free parameters. At each spatial frequency, the amplitude of the fitted sinusoid, A(ω), was taken as $STF^{m}(\omega)$ (Fig. 6j).

To interpret the measured STFs, we considered four different model scenarios: single cone RF centers with and without residual defocus in the AOSLO apparatus, and multiple cone RF centers with Gaussian weighting, with and without AOSLO residual defocus. For each scenario, the model was fit to the STF data of an examined RGC at multiple positions within the model cone mosaic and the final model was selected as the one with the minimum RMSE over the examined positions. The multi-position model fitting/selection was performed to take into account local inhomogeneities of the cone mosaic as exact RF center of each recorded RGC is only known to reside approximately within the central 40 microns. Details of the model fitting differences between each scenario, model training, and comparisons between the modeled cone mosaic and

464 the measured mosaic from M3 are provided in the Supplement (see **S4 Fig, S5 Fig, S6 Fig, S7 Fig**).
465 All figures in the main body of the paper assume the single cone center with fixed residual 0.067
466 D defocus scenario, unless otherwise noted.
467
468 **Results**
469
470 ***In vivo* functional imaging of foveal RGCs.** In this study, optical stimulation of foveal cones elicits
471 the activity of retinal ganglion cells in the living macaque eye. Intravitreal injection of an adeno-
472 associated virus (7m8 or AAV2) with a promoter (ubiquitous CAG or RGC-specific) produced
473 expression of the calcium indicator GCaMP6f [65] in animal M1 and GCaMP6s [65] in animals M2
474 and M3. As previously reported, injections in all three animals produced expression in a ring of
475 RGCs surrounding and radiating out from the foveal avascular zone where the internal limiting
476 membrane is thin [66, 68, 96] (Fig. 1a). Stimuli were presented to the centermost foveal cones
477 while a 488 nm imaging laser stimulated fluorescence from GCaMP expressing RGCs in a
478 rectangular area placed either nasally or temporally relative to the cones. Fig. 2a-b show the
479 fluorescence response of a single RGC to a simple luminance flicker stimulus in time as well as the
480 resulting Fourier transform, which shows the cell responding primarily at the stimulus frequency.
481 Figure 2c shows that, under our stimulus paradigm, the imaging light did not stimulate foveal
482 cones and confound the recorded functional responses after a 561 nm adapting light was
483 presented to the foveal cones. In each animal, hundreds of RGCs were recorded simultaneously
484 using this paradigm, and we used the precision of the AOSLO system to return to the same cells
485 over multiple sessions spanning weeks to months.
486

487 **Fig 1. Stimulus presentation and recording paradigm.** In **(a)** the general stimulation paradigm is
488 shown. Background is an image of the retina of M3 using the blue reflectance imaging modality
489 of a Heidelberg Spectralis instrument. In false color green are GCaMP-expressing cells from M3
490 imaged using the blue autofluorescence modality of the same Spectralis instrument. When using
491 the AOSLO instrument, videos are captured within a rectangular field of view (white dashed line)
492 while stimuli (white circle) such as cone-isolating flicker or drifting gratings (which were
493 rectangular in shape and covered approximately the same area as the white circle) are presented
494 to and centered on the centermost foveal cone photoreceptors. A 488 nm imaging laser in the
495 AOSLO (blue rectangle) excites GCaMP-mediated fluorescent responses of ganglion cells
496 surrounding the foveal slope. **(b)** shows the recorded cone densities at the fovea of M3 and **(c)**
497 shows the ganglion cells segmented (green) at the innermost edge of the foveal slope in M3.
498
499 **Fig 2. Data collection from ganglion cells *in vivo*. (a)** shows the smoothed time course of a single
500 RGC fluorescence response to a 0.15 Hz luminance flicker stimulus. **(b)** shows the amplitude of
501 the Fourier transform of the response time course, recovering the response peak at the stimulus
502 frequency of 0.15 Hz (red dashed line). **(c)** shows the effect of the imaging light on cone-mediated
503 response to stimuli in 62 foveal RGCs. The 488 nm imaging laser which excites GCaMP
504 fluorescence can scatter to foveal cones and confound cone stimulation. If the imaging light is
505 turned on without adaptation to any light, there is a quick rise and slow falloff in fluorescence due
506 to cone responses feeding RGCs. However, if the 561nm stimulus laser (used for drifting gratings)
507 or LED white point (used for chromatic stimuli) is presented at a mean luminance of 2-2.5 µW
508 during a short 30s adaptation period prior to imaging onset, then there is no corresponding effect

509 of the imaging light confounding the fluorescence signal. In all recordings, an adaptation light
510 preceded each recording to prevent this transient effect of scattered light from the imaging laser.
511
512 **Reliability and precision of foveal RGC recordings.** Across multiple sessions, RGC somas were
513 recorded from over a range of soma locations between 1.2 and 3.5 degrees from the center of
514 the foveal avascular zone (FAZ). When averaging data across multiple experiments, only cells that
515 were visible in all experiments were used. In M3, a follow-up experiment examining only cone
516 density (Fig. 1b) found the center of the FAZ to be roughly 41 microns inferior and 51 microns
517 nasal from the peak cone density which agrees with the range of data reported from humans [14].
518 Based on detailed receptive field mapping performed by McGregor *et. al.* [16], the cones driving
519 the receptive fields of the cells examined in all three animals are likely to be located at
520 eccentricities less than 36 arcmin from the foveal center, or a retinal radius of 120 microns
521 calculated using the primate model eye [97] with the axial lengths of each animal (M1: 17.51 mm,
522 M2: 17.20 mm, M3: 16.56 mm). According to the same mapping, the receptive fields of the
523 innermost cells we recorded from in M3 (Fig. 1c) are likely to be driven by cones found at
524 eccentricities less than 6 arcmin, or a retinal radius of 20 microns calculated using the same
525 primate model eye and the axial length of M3 (16.56 mm). All visual stimuli delivered to foveal
526 cones were large enough to cover both the FAZ center and the location of maximum cone density
527 and were some 10-60% larger than the cone area servicing even the furthest cells we recorded
528 from, ensuring the best possible chance of recording responses from the maximum number of
529 RGCs.
530
531 Functional measurements of RGCs made in the past often involved flashed stimuli and marking
532 approximate estimates of soma location on fundus images of the retina [e.g. 9, 98], a method that

533 leads to uncertainty about precise locations. In contrast, our imaging method captures
534 photoreceptors, vasculature, and RGC somas in the same field of view, allowing more accurate
535 measurements of receptive field eccentricity and soma position. One shortcoming of *in vivo*
536 functional imaging compared to traditional electrophysiology is that the excitation and imaging
537 sources can interfere with stimulation or fluorescence detection. However, unlike in the
538 periphery, foveal RGCs are displaced laterally from their photoreceptor inputs [1, 11, 15, 99].
539 Thus, our paradigm avoids this pitfall, and we can reliably image foveal RGCs without the 488 nm
540 excitation light stimulating foveal cones (Fig. 2c) or the photoreceptor stimuli interfering with the
541 RGC GCaMP fluorescence imaging.
542
543 **Chromatic tuning of foveal RGCs.** For functional classification of RGCs with receptive fields at the
544 foveal center, chromatic tuning was measured across multiple imaging sessions. Amplitude and
545 phase responses (Fig. 3a-d) to spatially uniform 0.15 Hz or 0.20 Hz flicker modulations that were
546 directed along a combination of L, M, L-M, S, and achromatic/luminance directions in color space
547 enabled reliable identification of chromatic tuning of RGCs in all three animals. For each cell, the
548 raw fluorescence time course was measured in response to each visual stimulus, and the Fourier
549 transform was used to find the cell's response amplitude at the stimulus frequency. The signal-
550 to-noise (SNR) response metric was calculated as the response Fourier amplitude (signal) minus
551 the mean amplitudes of higher spatial frequencies (noise), all divided by the standard deviation
552 of the noise. This analysis revealed several functional groups including L-M and M-L opponent
553 cells, S-ON and S-OFF cells, ON and OFF luminance cells, and cells with mixed L vs. M ± S responses.
554 In M3, single cone isolating stimuli were presented to the fovea and the individual cone weights
555 feeding RGCs were calculated as was done previously in LGN [60] (Fig. 4a-b). This analysis
556 estimates the relative contribution of each cone class to the response of a cell and revealed

557 further diversity of functional groups, including cells with responses to only L or M cones, as well
558 as various S cone connections to cells with either L or M cone input that were not L vs. M
559 opponent.
560
561 **Fig 3. Chromatic response properties of RGCs from three different animals.** Black dots show
562 luminance only responding cells, red dots show L-M and M-L cone opponent cells, blue dots show
563 S responding cells, while magenta dots show cells that responded to both L-M and S stimuli.
564 Dotted lines show the significance cutoff of SNR = 2 calculated based on cell responses to the
565 control stimulus (see Methods). Cell response is captured by our signal-to-noise metric described
566 in the Methods. Response phases were also calculated but are not directly shown; however,
567 positive SNRs correspond to responses that were in phase with the stimulus (ON response), while
568 negative SNRs correspond to responses that were approximately 180 deg out of phase with the
569 stimulus (OFF response). The luminance axis is perpendicular to the plane shown and is not
570 included for readability and because not all cells responded to the luminance stimulus. Luminance
571 only cells shown in black thus include both ON and OFF cells. In **(a)**, responses from 15 cells in M1
572 are shown after presentation of spatially uniform luminance, L-M isoluminant and S-isolating
573 stimuli at 0.2 Hz. In **(b)**, responses from 126 cells in M2 are shown after presentation of spatially
574 uniform luminance, L-M isoluminant and S-isolating stimuli at 0.2 Hz. In **(c)**, responses from 83
575 cells (a subset of the cells in Fig 4a) in M3 are shown after presentation of spatially uniform
576 luminance, L-isolating, M-isolating, and S-isolating stimuli at 0.15 Hz. In **(d)**, responses from 22
577 cells (a subset of the cells in Fig 4b) serving the very central fovea of M3 are shown after
578 presentation of spatially uniform luminance, L-isolating, M-isolating, and S-isolating stimuli at 0.15
579 Hz. These cells are closer to the foveal center than any of the cells shown in (c). In **(c-d)**, all stimuli

580 were single-cone isolating, so the L-M axis is calculated from the single cone L-isolating and M-
581 isolating responses and their relative phase.
582
583 **Fig 4. Cone weights of RGCs from M3.** The horizontal axis shows L cone weight, the vertical axis
584 the M cone weight, and the distance from the origin shows the S cone weight where further away
585 from the origin corresponds to less S-cone weighting. In **(a)**, 100 RGCs (a superset of the cells in
586 Fig 3c) were recorded across the entire width of the GCaMP-expressing ring in M3. There were 3
587 cells that only showed S cone responses, represented by overlapping circles at the origin. There
588 were also 4 L+M and 11 -L-M luminance only cells that are represented by asterisks in the upper
589 right and lower left. Because these cells only responded to the luminance stimulus but not the L-
590 isolating or M-isolating stimulus, the response sign is known but not the exact L or M cone
591 weighting. In **(b)**, 34 cells (a superset of the cells in Fig 3d) at the innermost edge of the foveal
592 slope in M3, served by the centermost foveal cones, were recorded from. No consistent S only
593 responses were observed, and there were 5 L+M and 2 -L-M luminance only cells.
594
595 **Identification of foveolar midget RGCs using chromatic tuning.** Across all three animals, cells with
596 L-M or M-L chromatic opponent responses (and no response to S-cone stimuli) were identified as
597 putative midget RGCs. There were a large number of these cells as can be seen in Figures 3,4: the
598 proportions of these putative midget cells were 44% (95% CI true proportion of 44±17%) of
599 responsive RGCs closest to the fovea (1.2-1.8 deg soma locations) in M3 (small imaging FOV), 33%
600 (95% CI true proportion of 33±9%) of responsive RGCs over the entire measured range in M3
601 (large imaging FOV), 72% (95% CI true proportion of 72±8%) of responsive RGCs in M2 (large
602 imaging FOV), and 47% (95% CI true proportion of 47±25%) of responsive RGCs in M1. It is
603 expected that midget RGCs comprise some 70-90% of foveal cells [20, 51, 99], and the confidence

604 intervals in M1 and M2 contain values in that range. In M3, single cone isolating stimuli were
605 used as detailed in the chromatic stimuli section—it is expected that these stimuli produce lower
606 responses in the classical cone opponent model of midget RGCs by not driving the center and
607 surround in counterphase as would the isoluminant L-M stimulus used in M1 and M2. There were
608 many cells in M3 (an additional 35% of the closest foveal RGCs, and an additional 32% over the
609 entire measured range) with only an L cone response or only an M cone response and no S cone
610 response. It is possible that some of these cells are cone opponent, but that the single cone
611 isolating stimuli produced too small of a response from the antagonistic surround in those cases.
612 Based on this uncertainty, we cannot say for sure whether the observed number of putative
613 midget RGCs in M3 is outside the range of expected values.
614
615 Soma size is a useful anatomical measure for distinguishing more peripheral ganglion cell types
616 and was examined here as a potential correlate with our putative midget RGCs. RGC soma sizes
617 were measured by two different observers see (Supplement **S1 Fig.**) using different methods, but
618 as others have reported, soma sizes did not exhibit bimodalities near the fovea [46]. Soma size
619 also did not distinguish between functional groups identified by chromatic tuning (Wilcoxon
620 ranksum test, $p > 0.1$ for comparisons between L-M, S only, luminance only, and L-M/S cells).
621
622 **Spatial tuning of foveolar putative midget RGCS.** Spatially patterned drifting gratings were used
623 to probe the spatial frequency response of RGCs and to augment measurements of chromatic
624 tuning (Fig. 5). In M3, at the small field of view focused on the innermost RGCs, a control and
625 drifting gratings of fourteen different spatial frequencies (561 nm, 6 Hz, 4-49 c/deg) were used to
626 stimulate foveal cones while the 488 nm imaging light elicited fluorescence from the same GCaMP
627 expressing RGCs shown in Figure 3d and Figure 4b. At this temporal frequency, GCaMP could not

track modulation, and responding cells exhibited a sustained increase in fluorescence in response to photoreceptor stimulation. A ΔF/F metric was calculated for each cell as the change in fluorescence under stimulation divided by the mean fluorescence in response to a grating of 17 c/deg (a spatial frequency with a robust response across the majority of the cells). Most of these putative midget RGCs at the foveal center in M3 (Fig. 5), which were all identified according to their L-M or M-L cone opponency, showed two salient features when their spatial frequency response functions were measured: a consistent and very strong low frequency cut, and a peak in the higher spatial frequencies (25-40 c/deg).

Fig 5. Spatial frequency responses of putative midget cells. Fifteen cells in M3 serving the central foveal cones were identified as L-M or M-L opponent (Fig. 3d). Each cell is numbered L1-11 or M1-4 based on whether the suspected center cone was an L or M cone. The green points (squares), blue points (triangles), and red points (circles) are measurements from three different experiments each one week apart. The solid orange line in each panel is the average response for that particular cell across all three experiments. The vertical axis is a response metric where the mean baseline fluorescence is subtracted from the fluorescence under stimulation and divided by the fluorescence under stimulation at the peak spatial frequency (see Methods). The error bars show the standard error at each data point, which represents the error in obtaining the signal and background needed to calculate the metric. Additional spatial frequency responses of cells from the large imaging FOV (**S2 Fig**) and non-midget RGCs (**S3 Fig**) can be found in the supplement.

Modeling of foveal midget RGCs. Using the ISETBio-based approach described in the Methods and depicted schematically in Figure 6, we derived estimates of the spatial RF organization from the measured STF data under four different model scenarios involving combinations of residual

652 instrument defocus (zero or some residual defocus) and RF center composition (single or multiple
653 cone inputs). Model cone mosaics matched well in both density and cone size with the measured
654 data in M3 along the horizontal and vertical meridians (see supplement **S4 Fig**). Modeling results
655 from one RGC are depicted in Figure 7. Figure 7a shows results from the modeling scenario that
656 assumes a single cone in the RF center and zero residual defocus. Note that this scenario predicts
657 a diffuse surround and that the derived STF does not agree well with the measured STF, resulting
658 in the largest RMSE across the four examined model scenarios. The STFs derived by the remaining
659 three modeling scenarios match the measured STF approximately equally well even though the
660 resulting cone pooling weights differ. The single cone RF center with 0.067 D residual defocus (Fig.
661 7b) results in a more focal surround than would be true if there were no residual defocus. The
662 multi-cone center RF with zero residual defocus (Fig. 7c) results in a diffuse RF center and a
663 surround that is marginally more diffuse than the center, which is not consistent with known
664 anatomy of foveal midget RFs. Finally, the multi-cone center 0.067 D residual defocus scenario
665 (Fig. 7d) results in an RF center with heavy input from one cone and very weak input from nearby
666 cones, and a focal surround. This scenario essentially collapses to the single cone center/0.067 D
667 residual defocus scenario. In Fig. 7e-f, the single and multi-cone RF center scenario performances
668 are depicted as a function of assumed residual defocus. Note that for the particular cell shown,
669 the minimal error in the single cone center scenario was at 0.077 D of residual defocus, and that
670 the multi-cone scenario never performs better than the best single cone scenario at all residual
671 defocus values modeled. Across all cells examined, the best performance for the single cone RF
672 center scenario was obtained for values of residual defocus between 0 D and 0.082 D with a mean
673 value of 0.067 D. The comparison shown for one cell in Fig. 7e-f is provided for all cells modeled
674 in Supplement **S6 Fig**. In addition, a cross-validation analysis (Supplement **S5 Fig**) similarly
675 suggests that across all cells, the data do not reject the single cone RF center/0.067 D model

relative to the multi-cone center models. Therefore, for the remainder of this paper, we use the single cone RF center/0.067 D residual defocus scenario as the vehicle for interpreting the measured STFs.

Fig 6. Schematic overview of the ISETBio modeling approach. To interpret the AOSLO-based STF measurements (Fig. 5) in terms of the spatial pooling of cone signals to the measured RGCs we model the spatial, spectral and temporal aspects of the stimulus, the optics, the cone mosaic and the cone pooling within the center and surrounds mechanisms of an RGC using the ISETBio toolbox. **(a)** A frame of the drifting monochromatic grating stimulus which is projected through the AOSLO system to stimulate and measure the GCaMP fluorescence – based spatial transfer function (STF) of RGCs, $STF^{\Delta F/F}(\omega)$ **(b).** The drifting grating is modeled as a temporal sequence of spatial spectral radiance scenes. These scenes model the AOSLO display including a diffraction-limited optical system with a 6.7 mm pupil **(c)** combined with residual defocus in the eye's wave aberrations **(d).** The resulting sequence of retinal irradiance maps are spectrally integrated and spatially averaged within the apertures of cones in a model of the animal's cone mosaic **(e)**, resulting in a spatiotemporal sequence of cone excitations **(f).** Cone excitations are transformed to cone modulations by first subtracting and subsequently dividing the mean cone excitation level **(g).** Modulation signals from different cones are scaled by the spatial weights with which the RF center and the RF surround mechanism pool cone signals **(h).** The weighted cone signals are subsequently summed **(i)** to compute the temporal response of the model RGC. A sinusoid is fitted to the RGC temporal response **(j)** and the amplitude of the sinusoid is taken as the STF of the model RGC at the stimulus spatial frequency, $STF^{m}(\omega)$. The RMSE between $STF^{m}(\omega)$ and $STF^{\Delta F/F}(\omega)$ **(k)** is minimized using a multi-start solver which optimizes the center and surround peak

699 sensitivity and radius parameters **(l)** of a difference of Gaussians (DoG) RF model **(m).** The model
700 yields the best-fitting cone pooling weights for the RGC.
701
702 **Figure 7. Model interpretation of measured STF for a single RGC. a-b** show single cone center
703 receptive field models with zero and 0.067 D residual defocus respectively. **c-d** show multi cone
704 center receptive field models with zero and 0.067 D residual defocus respectively. In a – d, the
705 first and second columns depict cone pooling weights for the center and surround mechanism,
706 derived by fitting the model STF to the measured STF. The third column depicts the integrated
707 (along the y-axis) center and surround sensitivity profiles, and the fourth column depicts the
708 model-predicted STF (orange lines) together with the measured STF (green disks). **e-f** show single
709 and multi-cone model residual errors for this particular cell with varying levels of residual defocus.
710 The best residual defocus for individual cells in the single cone center receptive field modeled
711 varies slightly, so 0.067 D was chosen as the value optimizing models across all cells measured.
712
713 Figure 8 depicts the results of the single-cone RF center/0.067 D scenario for four cells from the
714 center of the fovea of M3. These cells were chosen to showcase the model's fitting to slightly
715 different STF shapes and are not necessarily special in any way. Full results of the model fitting to
716 all 15 cells, including fits for all four scenarios examined, can be found in Supplement **S7 Fig**.
717
718 **Figure 8. ISETBio model receptive field estimates for four additional RGCs.** Each row shows the
719 model fits to a different cell's STF using the single cone center/0.067D residual defocus model.
720

721 The ISETBio model expresses the RFs directly in terms of the weights with which they pool signals
722 from cones in the mosaic, and as such is appropriate for comparison with anatomical
723 measurements and with *in vitro* physiological data where the optics of the eye are not in the
724 stimulus light path. In order to compare our data to other *in vivo* data collected in macaque [e.g.
725 9], where the eye's optics form a blurred image of the visual stimulus, we predicted *in vivo* STFs
726 using the cone pooling weights obtained from the single cone RF center/0.067 D residual defocus
727 scenario. To do so, we swapped the AOSLO optics with the animal's (M3) own wavefront
728 aberration optics as measured *in vivo* and assumed a pupil diameter of 2.5 mm. These
729 physiological optics STFs were computed for 100% contrast achromatic sinusoidal gratings, which
730 matched in their spatial and temporal properties the monochromatic gratings used to measure
731 the STFs in the AOSLO. Results of this analysis are displayed in Figure 9, with three example cells
732 shown in Figure 9a. Here, gray disks and black lines depict the AOSLO STF data and corresponding
733 fit of the model for the AOSLO measurement conditions (single cone RF center/0.067 D residual
734 defocus). Red disks depict the STFs computed using the model combined with M3's optics, and
735 red lines depict a simple DoG model fit to the computed STFs, as is typically done in analysis of *in*
736 *vivo* data. Note that the STFs predicted under physiological optics differ substantially from the
737 STFs obtained under near diffraction-limited optics: their magnitude is lower, and their shape is
738 less bandpass. They have weaker attenuation at low frequencies and peak at lower spatial
739 frequencies. This is due to the differential effect of the optical modulation transfer function (MTF)
740 to the STF of the center and surround mechanism, as illustrated in Figure 9b. The left panel depicts
741 the STFs of the center (pink) and surround (blue) mechanism of a model RGC under diffraction-
742 limited optics, and the gray disks represent the corresponding overall STF of the cell. The middle
743 panels depict MTFs for three hypothetical physiological optical systems with increasing amounts
744 of Gaussian blur. The physiological STFs that would be obtained under the three MTF conditions

745 are depicted in the right panels of Figure 9B. Note that as the physiological optics become more
746 blurred, the mapped STF becomes less bandpass and its peak shifts towards lower spatial
747 frequencies. This occurs because the difference between center STF and surround STF decreases
748 as the optics become more blurred. Also note the overall decrease in the magnitude of the STF
749 predicted under physiological optics conditions.
750
751 **Figure 9. Effect of physiological optics on RGC STFs. a.** Gray disks depict STF data measured using
752 the AOSLO for three RGCs, and the black lines show the STFs from the ISETBio model fit to these
753 cells. The cone weights from the model fits are used to predict the STF that would be measured
754 under the animal's own physiological optics (as characterized by wavefront-aberration
755 measurements taken during the experiment) with a 2.5 mm pupil. These model-predicted STFs
756 are depicted by the red disks. A simple DoG model is then fitted to the predicted STF data (red
757 line) for comparison to measurements obtained in traditional *in vivo* neurophysiological
758 experiments (e.g. Croner & Kaplan [9]). **b. Demonstration of the effect of physiological optics on**
759 **the STF.** The left panel depicts the STFs of the RF center and the RF surround of a model RGC as
760 they would be measured using diffraction-limited optics (pink and blue, respectively), whereas
761 the composite STF is depicted by the gray disks. The middle panels depict the MTFs of three
762 hypothetical physiological optical systems with progressively larger Gaussian point spread
763 functions. The corresponding STFs that would be measured under these physiological optical
764 systems are depicted in the right panels. Note the difference in scale between left y-axis (for the
765 center and surround STFs) and right y-axis (for composite STFs).
766
767 To compare our data with published results on midget RGC STFs obtained *in vivo* from outside the
768 central fovea, we fit the DoG model to the synthesized STFs obtained under the animal's optics

769 and we contrasted the DoG parameters derived using the procedure illustrated in Figure 9a to
770 those reported by Croner & Kaplan [9]. Figure 10 shows the characteristic radii of centers and
771 surrounds of data from M3, as predicted with physiological optics, along with data from Croner &
772 Kaplan. Cone characteristic radii as measured in M3 (blue circles) along with those obtained in
773 *Macaca nemestrina* from Packer *et al.* [100] (blue dashed line) are also shown. The midget RGC
774 center and surround characteristic radii from M3 lie along a reasonable extrapolation from the
775 Croner & Kaplan data which overall follows the general slope of the decreasing cone characteristic
776 radii. This supports the hypothesis that the midget pathway is specialized to preserve information
777 at the level of the cone photoreceptor mosaic, and that midget RGCs at the foveola transmit high
778 acuity chromatic information from retinal images.
779
780 Figure 11a depicts population data for R_c/R_s, the ratio of center to surround characteristic radii,
781 which typically shows a smaller center size compared to the surround in the Gaussian model and
782 can vary across RGC types. The data of Croner & Kaplan [9], which were obtained from a wide
783 range of eccentricities, are depicted in gray, whereas data from our foveal RGCs are shown in blue
784 (AOSLO optics) and yellow (M3 as predicted for physiological optics). Note that our population of
785 foveal RGCs has a higher mean R_c/R_s ratio (0.32 under AOSLO, 0.45 under M3 optics) than the
786 population of Croner & Kaplan (0.15), which is not surprising since foveal RGCs are expected to
787 have smaller surrounds than peripheral cells [6, 8, 20].
788
789 Figure 11b depicts population data for K_s/K_c, the ratio of surround to center peak sensitivity, a
790 measure of the surround compared to the center strength weighting, where typically it has been
791 found that the surrounds are much weaker than the centers when expressed in terms of peak
792 sensitivity [9]. Again, there is a difference between our foveal cells with mean K_s/K_c values of 0.28

793 under AOSLO optics and 0.11 under M3's optics, whereas the Croner & Kaplan data have a mean
794 of 0.0094. To the extent that the midget RGC data from M3 and the Croner & Kaplan study [9] are
795 comparable, this suggests that the surround strength expressed as a peak sensitivity ratio is
796 stronger at the foveola than at more eccentric locations, supported by the general trend of the
797 K_s/K_c ratio as a function of eccentricity in both the Croner & Kaplan and M3 data.
798
799 Figure 11c provides the surround/center integrated sensitivity ratio, which is essentially the ratio
800 of the total sensitivities (in a volumetric sense) of surrounds and centers. This does not vary with
801 eccentricity in the Croner & Kaplan data [9], as the variation in R_c/R_s and the variation of K_s/K_c
802 counteract each other such that the integrated sensitivity ratio is relatively constant across midget
803 cells. Consistent with this, the integrated sensitivity ratio for M3 predicted for physiological optics
804 conditions is similar to that found in Croner & Kaplan's data (means of 0.71 and 0.54 respectively).
805 Note also the large effect that the optics have on this value, which rises to 3.37 under the
806 measured AOSLO conditions. Overall, this population analysis shows that our foveal RGCs have a
807 large degree of surround antagonism when the receptive field is expressed directly in terms of
808 how the center and surround draw on the cones in the mosaic, but that this antagonism is greatly
809 attenuated under physiological optics viewing conditions, resulting in center/surround structure
810 in our data that is consistent with what has been observed in previous midget RGC studies across
811 a wide range of eccentricities.
812
813 **Figure 10. Comparison to extra-foveal *in vivo* midget RGC data.** Data from M3 model fits are
814 compared with extra-foveal data from Croner & Kaplan [9]. Gray circles and squares respectively
815 show center and surround characteristic radii from Croner & Kaplan as a function of eccentricity,
816 while pink circles and green squares show characteristic radii of centers and surrounds from M3

817 predicted using the ISETBio model with physiological optics accounted for. Light blue dashed line
818 shows cone characteristic radii data from Packer *et. al* [99]., while blue dots represent cone
819 characteristic radii measured in foveal cones of M3.
820
821 **Figure 11. Relationship between our findings in foveal midget RGCs and findings in midget RGCs**
822 **from earlier studies.** Data from Croner & Kaplan [9] is shown in gray, data from M3 using the
823 ISETBio model and physiological optics is shown in yellow, and data from M3 using the AOSLO
824 optics is shown in blue. **a.** Analysis of Rc/Rs ratio. Left panel: relationship between the Rc/Rs ratio
825 and retinal eccentricity. Right panel: distribution of Rc/Rs. The mean Rc/Rs ratio in the Croner &
826 Kaplan data is 0.15, vs. 0.45 in our foveal RGCs under physiological optics, and 0.32 in our foveal
827 RGCs under AOSLO optics. **b.** Analysis of Ks/Kc ratio. The mean Ks/Kc ratio in the Croner & Kaplan
828 data is 9.4e-3, vs. 1.1e-1 in our foveal RGCs under physiological optics, and 0.28 in our foveal RGCs
829 under AOSLO optics. **c.** Analysis of integrated surround-to-center ratio, $(Ks/Kc) \times (Rs/Rc)^2$. The
830 mean integrated surround-to-center ratio in the Croner & Kaplan data is 0.54, vs. 0.71 in our
831 foveal RGCs under physiological optics, and 3.37 in our foveal RGCs under AOSLO optics.
832
833 **Discussion**
834 In this study, we repeatedly imaged the same RGCs serving the foveal center *in vivo*, in three
835 animals, returning to the same retinal locations each time. Spatially uniform chromatic visual
836 stimuli enabled the identification of L-M and M-L opponent cells which were further interrogated
837 in one animal with drifting gratings of various spatial frequencies. Detailed modeling revealed
838 how the receptive fields of these RGCs draw on the cones of the retinal mosaic. The L vs. M
839 opponency and high spatial frequency responses of these cells identifies them as candidate
840 midget RGCs. Our modelling is consistent with the hypothesis that these cells have single cone

841 center inputs and are specialized to preserve the resolution of the cone photoreceptor mosaic in
842 the signals they send to the visual cortex.
843
844 **Measuring the precise location of cells from the foveal center.** In our data, the foveal avascular
845 zone (FAZ) was used as the 'center' measurement of the fovea, as the imaging paradigm precluded
846 using the location of maximum photoreceptor density for all sessions. The preferred retinal locus
847 of fixation (PRL) is also of interest but could not be determined using our method, since the
848 animals are anesthetized during the experiments and cannot freely fixate. The center of the
849 ganglion cell ring surrounding the fovea is also sometimes used to define the center of the fovea,
850 but this measure is highly correlated with the center of the FAZ [11, 101]. A more sophisticated
851 measure of the 'physiological center' can be identified using white noise stimuli as in McGregor
852 *et. al.* [16], but those stimuli were not used in this study. Others have characterized the precise
853 nature of the relationship between these various measures [14], and as noted in the results, our
854 measurements of the difference between the center of the FAZ and the location of maximum
855 cone density in M3 are in agreement with that literature. In any case, the difference in
856 identification of the 'foveal center' is not large enough under our method to affect the conclusion
857 that, using the mapping of McGregor *et. al.* [16], the receptive fields we examined are located
858 near the very center of the foveola.
859
860 **S-cone mediated color vision in the fovea.** As shown in Figures 3,4, cells with either S cone input
861 without L vs. M cone opponency (pure) or S cone input on top of L vs. M opponency (mixed) were
862 observed in each animal. 40% of responsive cells exhibited pure S responses and 7% mixed in M1,
863 9% pure and 14% mixed in M2, 16% pure and 3% mixed in the near fovea of M3 (large imaging
864 FOV), while no consistent S cone responses were recorded from the centermost foveolar cells

865 (small imaging FOV) in M3. Other than in M1 where the sample size was only 15 cells, these
866 numbers are consistent with the expected S cone density of approximately 10% across primate
867 fovea [102] and the known reduction of S cone density at the very center of the primate fovea [8,
868 15]. Others have reported subtypes of midget RGCs with S cone input or even that midget RGCs
869 may indiscriminately contact S cones along with L and M cones in the surround [4, 17, 48, 103,
870 104]. Our current data set has no repeatable S cone responses for RGCs at the innermost foveal
871 edge in M3, where RGCs are optically well-isolated, so we cannot rule out that the mixed cells we
872 measure are partially or fully the product of optical crosstalk resulting from the 25-30µm axial
873 resolution of the AOSLO instrument.
874
875 **Putative parasol cells at the fovea.** As shown in Figures 3,4, cells with no chromatic responses but
876 only a L+M or -L-M luminance response were recorded from each of the three animals: 7% of
877 responsive cells in M1, 4% in M2, 15% in the entirety of M3 and 20% of the centermost foveal
878 cells in M3, consistent with expected proportions of parasol ganglion cells, which are known to
879 mediate achromatic vision [20]. Simple modeling based on hexagonal packing of cones and
880 random wiring of 6 cones to midget surrounds suggests that approximately 9% of midget RGCs
881 could be dominated by a single cone type and appear achromatic (Supplement **S8 Fig.**). It is
882 probable then that some of these achromatic cells are midget RGCs but that most of them are
883 candidate parasol cells, though at this time we cannot make that distinction for an individual cell.
884 The spatial frequency response properties of these cells were even more varied than the
885 chromatic opponent cells (Supplement **S3 Fig.**), suggesting that they might be responsible for a
886 wide range of achromatic or even temporal vision properties that complement the midget system.
887 As noted in the results, we have not found significant differences between soma sizes of putative

888 foveal parasol and midget RGCs, so additional anatomical information such as histological studies
889 may be required in the future to confirm functional designations.
890
891 **The role of midget RGCs in foveal vision.** Among the putative midget RGCs from M3 (Fig. 5,7-9),
892 there was some variability among the responses to spatial frequencies in that a subset of cells
893 possessed lower spatial frequency response peaks (0-20 c/deg) compared to the peak spatial
894 frequencies of the majority of the cells (20-40 c/deg), though both of these groups of cells were
895 well fit by the single-cone RF center/0.067 D residual defocus model scenario, suggesting that the
896 change in their peak spatial frequency is related to the surround size and/or ratio of center and
897 surround strengths, as opposed to the spatial extent of the center. Previous studies examining
898 parvocellular neurons in the lateral geniculate nucleus (LGN) serving the central five degrees of
899 retina found an average of 4.57±2.75 c/deg as the peak spatial frequency response [62], and other
900 studies in the retina found parvocellular cells in the central five degrees to have a peak spatial
901 frequency response around 3 c/deg [9]. However, these previous studies relied on presenting
902 stimuli through the animals' optics, whereas the adaptive optics method we use approaches near
903 diffraction-limited stimulus presentation with some possible residual defocus. Indeed, as shown
904 in Figures 9,10, when the animal's optics are added back into a simulation of our data from M3,
905 we recover the classically measured bandpass shape and lower spatial frequency peaks that are
906 expected of parvocellular neurons (midget RGCs). We thus measure putative midget RGCs not
907 only closer to the foveal center and with greater precision than previously achievable, but also
908 with diminished optical blur in the *in vivo* retina compared to previous studies, with the exception
909 of studies that used interferometric stimuli to bypass the optics altogether [e.g. 10]. We thus posit
910 that the parameters of spatial DoG models fit to data collected through the optics do not directly
911 represent the *in situ* characteristics of RGCs, and that future *in vivo* measurements and models

912 need to take into account the effects of diffractive and optical blurring on the measured spatial
913 transfer functions.
914
915 In all 15 L-M and M-L cone opponent RGCs serving the central foveola, we could not reject the
916 hypothesis that the receptive fields were best described by a single cone center with some
917 residual instrumental defocus (0.067 D). There were some cells where the single cone
918 center/0.067 D scenario was clearly the best fit, but for many cells several of the scenarios
919 performed similarly in terms of RMSE—full details for all scenarios can be found in Supplement
920 (**S7 Fig**)**.** We posit that since the fovea is specialized for high acuity vision, it must be capable of
921 extracting high spatial frequency information from natural scenes which are known to follow a
922 $1/f^2$ law [105] and are dominated by low frequency information. Our modeling that adds the
923 optics of M3 back into the predictions (Fig. 9) suggests that natural ocular aberrations reduce the
924 peak spatial frequency obtained under AOSLO conditions by a factor of three or more, which
925 means that high spatial frequency information is greatly reduced by ocular transmission. Thus, to
926 extract meaningful high spatial frequency information from natural scenes through the eye's
927 native optics, detectors that preserve information at the resolution of the cone photoreceptor
928 mosaic are required. It seems highly probable that the putative midget RGCs shown in Figures 5,8
929 are responsible for this resolution, as they have responses consistent with single cone receptive
930 field centers and most have spatial transfer functions that peak well into the 20-40 c/deg range
931 when measured with respect to a retinal image under AOSLO conditions. McMahon *et al.* [10]
932 measured the spatial frequency responses of parvocellular LGN cell centers near the foveola using
933 interference fringes, which are not subject to blur by diffraction. They found that cells still had
934 detectable responses to spatial frequencies above 100 c/deg, with some responses that were
935 complex and inconsistent with a simple difference of Gaussians model. Because the AO-corrected

936 stimuli used in the present study were subject to blur by diffraction, we were unable to explore
937 responses at the high spatial frequencies where such effects were observed.
938
939 Putative midget RGCs with the lowest spatial frequency peaks comprised only 2/15 cells (cells L2
940 and M3) compared to ones with higher spatial frequency peaks (13/15 cells). The two cells with
941 lowest spatial frequency peaks had stronger surround weighting compared to the centers (higher
942 K_s/K_c ratio) coupled with surrounds that were almost spatially coexistent with the centers. These
943 two cells are inconsistent with previous data finding the center responses of midget RGCs to be
944 some 10x-1000x stronger than those of the surround and finding centers to be much smaller in
945 spatial extent than surrounds [9]. The cells with higher spatial frequency peaks had center and
946 surround strength ratios closer to previous data, though all 15 cells had higher surround/center
947 integrated sensitivity ratios than previous results such as those reported by Croner & Kaplan [9].
948 These differences, however, are explainable by the blurring effect of the optics as presented in
949 Figures 9,10,11. Further study of low-frequency L-M and M-L cone opponent cells will confirm if
950 they exhibit any other physiological differences or if they belong to one or more of several midget
951 subtypes as others have postulated to exist [48, 103]. There is also evidence that parasol ganglion
952 cells can respond weakly to L vs. M modulation [106], but they are not expected to have single
953 cone centers from anatomy [6, 20, 27, 107], so it is unlikely that any of the 15 cells studied here
954 are parasols.
955
956 **Modeling foveal RGCs.** In our modeling, we could not reject the hypothesis that the 15 cells
957 studied from the center of the fovea in M3 had single cone centers with some residual optical
958 blur, beyond diffraction, present in the measurements. We think it likely that there was some
959 residual optical blur, and certainly cannot reject this idea. However, we note that model scenarios

960 that did not restrict to a single-cone center also describe the data, and that if no residual blur is
961 assumed then the single-cone center model can be rejected for some cells. There are two reasons
962 it is difficult to differentiate between single and multi-cone scenarios from our data. First, due to
963 limitations imposed by the pixel density of the raster scan, our measurements did not extend to
964 high spatial frequencies (>50 c/deg) where the different scenarios would make more clearly
965 different predictions. Second, there was inter-session variability in the measured STFs (Fig. 5),
966 which decreases the power of the data. In future experiments, we plan to (i) extend the range of
967 spatial frequencies examined and (ii) test multiple grating orientations. Despite these limitations,
968 as noted in the Supplement (**S7 Fig**), the multi-cone RF scenario with residual defocus often
969 produces a RF strikingly similar to the single-cone RF scenario with residual defocus, with only a
970 minimal amount of cone coupling, and the classical understanding of midget RGCs that postulates
971 single-cone centers is consistent with our data.
972
973 A notable observation of the STFs in our population of foveal RGCs (Fig. 8) is the large amount of
974 low-spatial frequency attenuation. Such observations are not typical of midget ganglion cells
975 reported in other *in vivo* studies [9]. The question then arises as to whether these most central
976 foveal cells have distinctively different RF organization from the less-foveal cells reported in other
977 studies, or whether the underlying RF organization is similar, but the measured data differ
978 between the two types of studies simply because of differences in the optical systems involved.
979 When the animal's optics are added back in (Figures 9,10,11), the STFs have a clear shift of peak
980 sensitivity towards lower spatial frequencies, approaching those of previous *in vivo* studies but
981 not exactly replicating them, suggesting that the optics account for most of the observed
982 differences with the possibility of modest foveal specialization or instrument differences
983 accounting for the rest.

984

985 The modeling used in this study has the capability to add a subject's optical PSF (here through the
986 measured wavefront aberrations from M3) to predict responses to stimuli presented through the
987 natural (non-AO-corrected) optics. The robust nature of the entire simulation allows for any cone
988 density profile or PSF to be substituted in the model so that the simulation can be generalized to
989 population data or be tailored to individual subjects, as it has been here for M3.

990

991 **Acknowledgments**

992

993 The authors would like to thank Amber Walker for performing animal anesthesia and monitoring
994 during imaging, Deniz Dalkara for providing the viral vector used in M1, Max Snodderly for
995 assistance with estimating the effect of macular pigment, Charles Granger for optical alignment
996 assistance, Daniel Guarino and Martin Gira for maintaining the stereotaxic cart and other
997 electronic components, as well as Aby Joseph, Jennifer Hunter, and Jesse Schallek for data analysis
998 suggestions. We thank the vector core at the Perelman School of Medicine, University of
999 Pennsylvania and the Genetically-Encoded Neuronal Indicator and Effector (GENIE) Project and
1000 the Janelia Research Campus of the Howard Hughes Medical Institute, specifically Vivek
1001 Jayaraman, Ph.D., Douglas S. Kim, Ph.D., Loren L. Looger, Ph.D., and Karel Svoboda, Ph.D.

1002

1003 **References**

1004 1. Schein SJ. Anatomy of macaque fovea and spatial densities of neurons in foveal
1005 representation. J Comp Neurol. 1988;269(4):479-505. Epub 1988/03/22. doi:
1006 10.1002/cne.902690403. PubMed PMID: 3372725.
1007 2. Wassle H, Grunert U, Rohrenbeck J, Boycott BB. Cortical magnification factor and the
1008 ganglion cell density of the primate retina. Nature. 1989;341(6243):643-6. Epub 1989/10/19.
1009 doi: 10.1038/341643a0. PubMed PMID: 2797190.

1010 3. Wassle H, Grunert U, Rohrenbeck J, Boycott BB. Retinal ganglion cell density and cortical
1011 magnification factor in the primate. Vision Res. 1990;30(11):1897-911. Epub 1990/01/01.
1012 PubMed PMID: 2288097.
1013 4. De Monasterio FM, Gouras P. Functional properties of ganglion cells of the rhesus
1014 monkey retina. J Physiol. 1975;251(1):167-95. Epub 1975/09/01. doi:
1015 10.1113/jphysiol.1975.sp011086. PubMed PMID: 810576; PubMed Central PMCID:
1016 PMCPMC1348381.
1017 5. Derrington AM, Lennie P. Spatial and temporal contrast sensitivities of neurones in
1018 lateral geniculate nucleus of macaque. J Physiol. 1984;357:219-40. Epub 1984/12/01. doi:
1019 10.1113/jphysiol.1984.sp015498. PubMed PMID: 6512690; PubMed Central PMCID:
1020 PMCPMC1193256.
1021 6. Watanabe M, Rodieck RW. Parasol and midget ganglion cells of the primate retina. J
1022 Comp Neurol. 1989;289(3):434-54. Epub 1989/11/15. doi: 10.1002/cne.902890308. PubMed
1023 PMID: 2808778.
1024 7. Kolb H, Dekorver L. Midget ganglion cells of the parafovea of the human retina: a study
1025 by electron microscopy and serial section reconstructions. J Comp Neurol. 1991;303(4):617-36.
1026 Epub 1991/01/22. doi: 10.1002/cne.903030408. PubMed PMID: 1707423.
1027 8. Hendrickson A. A morphological comparison of foveal development in man and monkey.
1028 Eye (Lond). 1992;6 (Pt 2):136-44. Epub 1992/01/01. doi: 10.1038/eye.1992.29. PubMed PMID:
1029 1624035.
1030 9. Croner LJ, Kaplan E. Receptive fields of P and M ganglion cells across the primate retina.
1031 Vision Res. 1995;35(1):7-24. Epub 1995/01/01. doi: 10.1016/0042-6989(94)e0066-t. PubMed
1032 PMID: 7839612.
1033 10. McMahon MJ, Lankheet MJ, Lennie P, Williams DR. Fine structure of parvocellular
1034 receptive fields in the primate fovea revealed by laser interferometry. J Neurosci.
1035 2000;20(5):2043-53. Epub 2000/02/24. PubMed PMID: 10684905.
1036 11. Hendrickson A. Organization of the Adult Primate Fovea. In: Penfold PL, Provis JM,
1037 editors. Macular Degeneration: Springer Berlin Heidelberg; 2005.
1038 12. Yin L, Masella B, Dalkara D, Zhang J, Flannery JG, Schaffer DV, et al. Imaging light
1039 responses of foveal ganglion cells in the living macaque eye. J Neurosci. 2014;34(19):6596-605.
1040 Epub 2014/05/09. doi: 10.1523/jneurosci.4438-13.2014. PubMed PMID: 24806684; PubMed
1041 Central PMCID: PMCPMC4012315.
1042 13. Sinha R, Hoon M, Baudin J, Okawa H, Wong ROL, Rieke F. Cellular and Circuit
1043 Mechanisms Shaping the Perceptual Properties of the Primate Fovea. Cell. 2017;168(3):413-
1044 26.e12. Epub 2017/01/28. doi: 10.1016/j.cell.2017.01.005. PubMed PMID: 28129540; PubMed
1045 Central PMCID: PMCPMC5298833.
1046 14. Wilk MA, Dubis AM, Cooper RF, Summerfelt P, Dubra A, Carroll J. Assessing the spatial
1047 relationship between fixation and foveal specializations. Vision Research. 2017;132:53-61. doi:
1048 https://doi.org/10.1016/j.visres.2016.05.001.
1049 15. Bringmann A, Syrbe S, Gorner K, Kacza J, Francke M, Wiedemann P, et al. The primate
1050 fovea: Structure, function and development. Prog Retin Eye Res. 2018;66:49-84. Epub
1051 2018/04/03. doi: 10.1016/j.preteyeres.2018.03.006. PubMed PMID: 29609042.
1052 16. McGregor JE, Yin L, Yang Q, Godat T, Huynh KT, Zhang J, et al. Functional architecture of
1053 the foveola revealed in the living primate. PLoS One. 2018;13(11):e0207102. Epub 2018/11/30.
1054 doi: 10.1371/journal.pone.0207102. PubMed PMID: 30485298; PubMed Central PMCID:
1055 PMCPMC6261564 following competing interests: DRW and WHM receive funding from the
1056 National Eye Institute. DRW receives additional funding from The Arnold and Mabel Beckman

Foundation and WHM receives funding from Research to Prevent Blindness as detailed in the Financial Disclosure statement. DRW has patents with the University of Rochester for adaptive optics imaging of the retina: US patent #6,199,986 "Rapid, automatic measurement of the eye's wave aberration". US patent #6,264,328 "Wavefront sensor with off-axis illumination" and US patent 6,338,559 "Apparatus and method for improving vision and retinal imaging". QY has patents with the University of Rochester, Canon Inc. and the University of Montana, for image stabilization algorithms: US patent #9,226,656: "Real-time optical and digital image stabilization for adaptive optics scanning ophthalmoscopy", US patent # 9,406,133: "System and method for real-time image registration", US patent #: 9,485,383, "Imaging based correction of distortion from a scanner" and US patent #: 9,454,084, "Light source modulation for a scanning microscope". Additionally QY has undertaken consultancy work for Oculus VR and Boston Micromachine Corporation. This does not alter our adherence to PLOS ONE policies on sharing data and materials.

17. Thoreson WB, Dacey DM. Diverse Cell Types, Circuits, and Mechanisms for Color Vision in the Vertebrate Retina. Physiol Rev. 2019;99(3):1527-73. Epub 2019/05/30. doi: 10.1152/physrev.00027.2018. PubMed PMID: 31140374; PubMed Central PMCID: PMCPMC6689740.

18. Dacey DM. The mosaic of midget ganglion cells in the human retina. J Neurosci. 1993;13(12):5334-55. Epub 1993/12/01. PubMed PMID: 8254378.

19. Dacey DM. Primate retina: cell types, circuits and color opponency. Prog Retin Eye Res. 1999;18(6):737-63. Epub 1999/10/26. doi: 10.1016/s1350-9462(98)00013-5. PubMed PMID: 10530750.

20. Dacey DM. Origins of Perception: Retinal Ganglion Cell Diversity and the Creation of Parallel Visual Pathways. In: Gazzaniga MS, editor. The Cognitive Neurosciences: The MIT Press; 2004. p. 281-302.

21. Hansen T, Pracejus L, Gegenfurtner KR. Color perception in the intermediate periphery of the visual field. J Vis. 2009;9(4):26.1-12. Epub 2009/09/18. doi: 10.1167/9.4.26. PubMed PMID: 19757935.

22. Leventhal AG, Rodieck RW, Dreher B. Retinal ganglion cell classes in the Old World monkey: morphology and central projections. Science. 1981;213(4512):1139-42. Epub 1981/09/04. doi: 10.1126/science.7268423. PubMed PMID: 7268423.

23. Perry VH, Cowey A. Retinal ganglion cells that project to the superior colliculus and pretectum in the macaque monkey. Neuroscience. 1984;12(4):1125-37. Epub 1984/08/01. doi: 10.1016/0306-4522(84)90007-1. PubMed PMID: 6483194.

24. Perry VH, Oehler R, Cowey A. Retinal ganglion cells that project to the dorsal lateral geniculate nucleus in the macaque monkey. Neuroscience. 1984;12(4):1101-23. Epub 1984/08/01. doi: 10.1016/0306-4522(84)90006-x. PubMed PMID: 6483193.

25. Kaplan E, Shapley RM. The primate retina contains two types of ganglion cells, with high and low contrast sensitivity. Proceedings of the National Academy of Sciences of the United States of America. 1986;83(8):2755-7. Epub 1986/04/01. doi: 10.1073/pnas.83.8.2755. PubMed PMID: 3458235; PubMed Central PMCID: PMCPMC323379.

26. Perry VH, Silveira LCL. Functional lamination in the ganglion cell layer of the macaque's retina. Neuroscience. 1988;25(1):217-23. doi: https://doi.org/10.1016/0306-4522(88)90020-6.

27. Dacey DM, Petersen MR. Dendritic field size and morphology of midget and parasol ganglion cells of the human retina. Proceedings of the National Academy of Sciences of the United States of America. 1992;89(20):9666-70. doi: 10.1073/pnas.89.20.9666. PubMed PMID: 1409680.

1104 28. Grunert U, Greferath U, Boycott BB, Wassle H. Parasol (P alpha) ganglion-cells of the
1105 primate fovea: immunocytochemical staining with antibodies against GABAA-receptors. Vision
1106 Res. 1993;33(1):1-14. Epub 1993/01/01. PubMed PMID: 8383899.
1107 29. Dacey DM. Morphology of a small-field bistratified ganglion cell type in the macaque
1108 and human retina. Vis Neurosci. 1993;10(6):1081-98. Epub 1993/11/01. doi:
1109 10.1017/s0952523800010191. PubMed PMID: 8257665.
1110 30. Dacey DM, Lee BB. The 'blue-on' opponent pathway in primate retina originates from a
1111 distinct bistratified ganglion cell type. Nature. 1994;367(6465):731-5. Epub 1994/02/24. doi:
1112 10.1038/367731a0. PubMed PMID: 8107868.
1113 31. Graham DM, Wong KY. Melanopsin-expressing, Intrinsically Photosensitive Retinal
1114 Ganglion Cells (ipRGCs). In: Kolb H, Fernandez E, Nelson R, editors. Webvision: The Organization
1115 of the Retina and Visual System. Salt Lake City (UT)1995.
1116 32. Dacey DM. Circuitry for color coding in the primate retina. Proceedings of the National
1117 Academy of Sciences of the United States of America. 1996;93(2):582-8. Epub 1996/01/23. doi:
1118 10.1073/pnas.93.2.582. PubMed PMID: 8570599; PubMed Central PMCID: PMCPMC40095.
1119 33. Lee BB. Receptive field structure in the primate retina. Vision Research. 1996;36(5):631-
1120 44. doi: https://doi.org/10.1016/0042-6989(95)00167-0.
1121 34. Calkins DJ, Tsukamoto Y, Sterling P. Microcircuitry and mosaic of a blue-yellow ganglion
1122 cell in the primate retina. J Neurosci. 1998;18(9):3373-85. Epub 1998/05/09. PubMed PMID:
1123 9547245; PubMed Central PMCID: PMCPMC6792640.
1124 35. Chichilnisky EJ, Baylor DA. Receptive-field microstructure of blue-yellow ganglion cells in
1125 primate retina. Nat Neurosci. 1999;2(10):889-93. Epub 1999/09/24. doi: 10.1038/13189.
1126 PubMed PMID: 10491609.
1127 36. Telkes I, Distler C, Hoffmann KP. Retinal ganglion cells projecting to the nucleus of the
1128 optic tract and the dorsal terminal nucleus of the accessory optic system in macaque monkeys.
1129 Eur J Neurosci. 2000;12(7):2367-75. Epub 2000/08/18. doi: 10.1046/j.1460-9568.2000.00133.x.
1130 PubMed PMID: 10947815.
1131 37. Dacey DM, Liao HW, Peterson BB, Robinson FR, Smith VC, Pokorny J, et al. Melanopsin-
1132 expressing ganglion cells in primate retina signal colour and irradiance and project to the LGN.
1133 Nature. 2005;433(7027):749-54. Epub 2005/02/18. doi: 10.1038/nature03387. PubMed PMID:
1134 15716953.
1135 38. Calkins DJ, Sterling P. Microcircuitry for two types of achromatic ganglion cell in primate
1136 fovea. J Neurosci. 2007;27(10):2646-53. Epub 2007/03/09. doi: 10.1523/JNEUROSCI.4739-
1137 06.2007. PubMed PMID: 17344402; PubMed Central PMCID: PMCPMC6672494.
1138 39. Petrusca D, Grivich MI, Sher A, Field GD, Gauthier JL, Greschner M, et al. Identification
1139 and characterization of a Y-like primate retinal ganglion cell type. J Neurosci.
1140 2007;27(41):11019-27. Epub 2007/10/12. doi: 10.1523/jneurosci.2836-07.2007. PubMed PMID:
1141 17928443.
1142 40. Field GD, Sher A, Gauthier JL, Greschner M, Shlens J, Litke AM, et al. Spatial Properties
1143 and Functional Organization of Small Bistratified Ganglion Cells in Primate Retina. The Journal of
1144 Neuroscience. 2007;27(48):13261-72. doi: 10.1523/jneurosci.3437-07.2007.
1145 41. Crook JD, Peterson BB, Packer OS, Robinson FR, Gamlin PD, Troy JB, et al. The smooth
1146 monostratified ganglion cell: evidence for spatial diversity in the Y-cell pathway to the lateral
1147 geniculate nucleus and superior colliculus in the macaque monkey. J Neurosci.
1148 2008;28(48):12654-71. Epub 2008/11/28. doi: 10.1523/jneurosci.2986-08.2008. PubMed PMID:
1149 19036959; PubMed Central PMCID: PMCPMC2778055.

1150 42. Percival KA, Martin PR, Grunert U. Organisation of koniocellular-projecting ganglion cells
1151 and diffuse bipolar cells in the primate fovea. Eur J Neurosci. 2013;37(7):1072-89. Epub
1152 2013/01/15. doi: 10.1111/ejn.12117. PubMed PMID: 23311464.
1153 43. Crook JD, Packer OS, Troy JB, Dacey DM. Synaptic Mechanisms of Color and Luminance
1154 Coding: Rediscovering the X-Y-cell dichotomy in primate retinal ganglion cels. . In: Werner JS,
1155 Chalupa LM, editors. The New Visual Neurosciences: The MIT Press; 2013. p. 123-44.
1156 44. Puller C, Manookin MB, Neitz J, Rieke F, Neitz M. Broad thorny ganglion cells: a
1157 candidate for visual pursuit error signaling in the primate retina. J Neurosci. 2015;35(13):5397-
1158 408. Epub 2015/04/04. doi: 10.1523/jneurosci.4369-14.2015. PubMed PMID: 25834063;
1159 PubMed Central PMCID: PMCPMC4381007.
1160 45. Liao HW, Ren X, Peterson BB, Marshak DW, Yau KW, Gamlin PD, et al. Melanopsin-
1161 expressing ganglion cells on macaque and human retinas form two morphologically distinct
1162 populations. J Comp Neurol. 2016;524(14):2845-72. Epub 2016/03/15. doi: 10.1002/cne.23995.
1163 PubMed PMID: 26972791; PubMed Central PMCID: PMCPMC4970949.
1164 46. Liu Z, Kurokawa K, Zhang F, Lee JJ, Miller DT. Imaging and quantifying ganglion cells and
1165 other transparent neurons in the living human retina. Proceedings of the National Academy of
1166 Sciences of the United States of America. 2017;114(48):12803-8. Epub 2017/11/16. doi:
1167 10.1073/pnas.1711734114. PubMed PMID: 29138314; PubMed Central PMCID:
1168 PMCPMC5715765.
1169 47. Peng YR, Shekhar K, Yan W, Herrmann D, Sappington A, Bryman GS, et al. Molecular
1170 Classification and Comparative Taxonomics of Foveal and Peripheral Cells in Primate Retina. Cell.
1171 2019;176(5):1222-37 e22. Epub 2019/02/05. doi: 10.1016/j.cell.2019.01.004. PubMed PMID:
1172 30712875; PubMed Central PMCID: PMCPMC6424338.
1173 48. Wool LE, Packer OS, Zaidi Q, Dacey DM. Connectomic Identification and Three-
1174 Dimensional Color Tuning of S-OFF Midget Ganglion Cells in the Primate Retina. J Neurosci.
1175 2019;39(40):7893-909. Epub 2019/08/14. doi: 10.1523/JNEUROSCI.0778-19.2019. PubMed
1176 PMID: 31405926; PubMed Central PMCID: PMCPMC6774400.
1177 49. Rhoades CE, Shah NP, Manookin MB, Brackbill N, Kling A, Goetz G, et al. Unusual
1178 Physiological Properties of Smooth Monostratified Ganglion Cell Types in Primate Retina.
1179 Neuron. 2019;103(4):658-72 e6. Epub 2019/06/23. doi: 10.1016/j.neuron.2019.05.036. PubMed
1180 PMID: 31227309; PubMed Central PMCID: PMCPMC6817368.
1181 50. Dacey DM, Kim YJ, Packer OS, Detwiler PB. ON-OFF direction selective ganglion cells in
1182 macaque monkey retina are tracer-coupled to an ON-OFF direction selective amacrine cell type.
1183 Investigative Ophthalmology & Visual Science. 2019;60(9):5280-.
1184 51. Kim US, Mahroo OA, Mollon JD, Yu-Wai-Man P. Retinal Ganglion Cells—Diversity of Cell
1185 Types and Clinical Relevance. Frontiers in Neurology. 2021;12(635). doi:
1186 10.3389/fneur.2021.661938.
1187 52. Grünert U, Martin PR. Cell types and cell circuits in human and non-human primate
1188 retina. Progress in Retinal and Eye Research. 2020;78:100844. doi:
1189 https://doi.org/10.1016/j.preteyeres.2020.100844.
1190 53. Lee BB, Martin PR, Valberg A. Sensitivity of macaque retinal ganglion cells to chromatic
1191 and luminance flicker. The Journal of physiology. 1989;414:223-43. doi:
1192 10.1113/jphysiol.1989.sp017685. PubMed PMID: 2607430.
1193 54. Lee BB, Pokorny J, Smith VC, Martin PR, Valberg A. Luminance and chromatic
1194 modulation sensitivity of macaque ganglion cells and human observers. J Opt Soc Am A.
1195 1990;7(12):2223-36. Epub 1990/12/01. doi: 10.1364/josaa.7.002223. PubMed PMID: 2090801.

1196 55. Soto F, Hsiang J-C, Rajagopal R, Piggott K, Harocopos GJ, Couch SM, et al. Efficient
1197 Coding by Midget and Parasol Ganglion Cells in the Human Retina. Neuron. 2020;107(4):656-
1198 66.e5. doi: https://doi.org/10.1016/j.neuron.2020.05.030.
1199 56. Brackbill N, Rhoades C, Kling A, Shah NP, Sher A, Litke AM, et al. Reconstruction of
1200 natural images from responses of primate retinal ganglion cells. eLife. 2020;9:e58516. doi:
1201 10.7554/eLife.58516. PubMed PMID: 33146609.
1202 57. Calkins DJ, Schein SJ, Tsukamoto Y, Sterling P. M and L cones in macaque fovea connect
1203 to midget ganglion cells by different numbers of excitatory synapses. Nature.
1204 1994;371(6492):70-2. doi: 10.1038/371070a0.
1205 58. Crook JD, Dacey DM. Circuitry and receptive field structure underlying 'double duty'
1206 performance by midget ganglion cells. Journal of Vision. 2010;10(15):5-. doi: 10.1167/10.15.5.
1207 59. Kaas JH, Guillery RW, Allman JM. Some Principles of Organization in the Dorsal Lateral
1208 Geniculate Nucleus; pp. 253–267. Brain, Behavior and Evolution. 1972;6(1-6):253-67. doi:
1209 10.1159/000123713.
1210 60. Derrington AM, Krauskopf J, Lennie P. Chromatic mechanisms in lateral geniculate
1211 nucleus of macaque. J Physiol. 1984;357:241-65. Epub 1984/12/01. doi:
1212 10.1113/jphysiol.1984.sp015499. PubMed PMID: 6512691; PubMed Central PMCID:
1213 PMCPMC1193257.
1214 61. Solomon SG, Peirce JW, Dhruv NT, Lennie P. Profound contrast adaptation early in the
1215 visual pathway. Neuron. 2004;42(1):155-62. Epub 2004/04/07. doi: 10.1016/s0896-
1216 6273(04)00178-3. PubMed PMID: 15066272.
1217 62. Levitt JB, Schumer RA, Sherman SM, Spear PD, Movshon JA. Visual response properties
1218 of neurons in the LGN of normally reared and visually deprived macaque monkeys. J
1219 Neurophysiol. 2001;85(5):2111-29. Epub 2001/05/16. doi: 10.1152/jn.2001.85.5.2111. PubMed
1220 PMID: 11353027.
1221 63. Gray DC, Merigan W, Wolfing JI, Gee BP, Porter J, Dubra A, et al. In vivo fluorescence
1222 imaging of primate retinal ganglion cells and retinal pigment epithelial cells. Optics express.
1223 2006;14(16):7144-58. Epub 2006/08/07. doi: 10.1364/oe.14.007144. PubMed PMID: 19529085.
1224 64. Yin L, Geng Y, Osakada F, Sharma R, Cetin AH, Callaway EM, et al. Imaging light
1225 responses of retinal ganglion cells in the living mouse eye. J Neurophysiol. 2013;109(9):2415-21.
1226 Epub 2013/02/15. doi: 10.1152/jn.01043.2012. PubMed PMID: 23407356; PubMed Central
1227 PMCID: PMCPMC3652215.
1228 65. Chen T-W, Wardill TJ, Sun Y, Pulver SR, Renninger SL, Baohan A, et al. Ultrasensitive
1229 fluorescent proteins for imaging neuronal activity. Nature. 2013;499(7458):295-300. doi:
1230 10.1038/nature12354. PubMed PMID: 23868258.
1231 66. Yin L, Greenberg K, Hunter JJ, Dalkara D, Kolstad KD, Masella BD, et al. Intravitreal
1232 injection of AAV2 transduces macaque inner retina. Invest Ophthalmol Vis Sci. 2011;52(5):2775-
1233 83. Epub 2011/02/12. doi: 10.1167/iovs.10-6250. PubMed PMID: 21310920; PubMed Central
1234 PMCID: PMCPMC3088562.
1235 67. Chaffiol A, Caplette R, Jaillard C, Brazhnikova E, Desrosiers M, Dubus E, et al. A New
1236 Promoter Allows Optogenetic Vision Restoration with Enhanced Sensitivity in Macaque Retina.
1237 Molecular therapy : the journal of the American Society of Gene Therapy. 2017;25(11):2546-60.
1238 Epub 2017/08/16. doi: 10.1016/j.ymthe.2017.07.011. PubMed PMID: 28807567; PubMed
1239 Central PMCID: PMCPMC5675708.
1240 68. McGregor JE, Godat T, Dhakal K, Parkins K, Strazzeri J, Bateman B, et al. Optogenetic
1241 restoration of retinal ganglion cell activity in the living primate. Nature Communications. 2020.

1242 69. Delori FC, Webb RH, Sliney DH. Maximum permissible exposures for ocular safety (ANSI
1243 2000), with emphasis on ophthalmic devices. J Opt Soc Am A. 2007;24(5):1250-65. doi:
1244 10.1364/JOSAA.24.001250.
1245 70. Schulmeister K. The upcoming new editions of IEC 60825-1 and ANSI Z136.1 – Examples
1246 on impact for classification and exposure limits. International Laser Safety Conference.
1247 2013;2013(1):330-7. doi: 10.2351/1.5056809.
1248 71. Rockwell B, Thomas R, Zimmerman S. Updates to the ANSI Z136.1 standard.
1249 International Laser Safety Conference. 2015;2015(1):75-7. doi: 10.2351/1.5056858.
1250 72. Geng Y, Dubra A, Yin L, Merigan WH, Sharma R, Libby RT, et al. Adaptive optics retinal
1251 imaging in the living mouse eye. Biomedical optics express. 2012;3(4):715-34. Epub 2012/05/11.
1252 doi: 10.1364/boe.3.000715. PubMed PMID: 22574260; PubMed Central PMCID:
1253 PMCPMC3345801.
1254 73. Atchison DA, Smith G. Chromatic dispersions of the ocular media of human eyes. J Opt
1255 Soc Am A. 2005;22(1):29-37. doi: 10.1364/JOSAA.22.000029.
1256 74. Nelder JA, Mead R. A Simplex Method for Function Minimization. The Computer Journal.
1257 1965;7(4):308-13. doi: 10.1093/comjnl/7.4.308.
1258 75. Rossi EA, Granger CE, Sharma R, Yang Q, Saito K, Schwarz C, et al. Imaging individual
1259 neurons in the retinal ganglion cell layer of the living eye. Proceedings of the National Academy
1260 of Sciences of the United States of America. 2017;114(3):586-91. Epub 2017/01/05. doi:
1261 10.1073/pnas.1613445114. PubMed PMID: 28049835; PubMed Central PMCID:
1262 PMCPMC5255596.
1263 76. Baron WS. Maxwellian view stimulator for electrophysiological or psychophysical work.
1264 Applied optics. 1973;12(11):2560-2. Epub 1973/11/01. doi: 10.1364/AO.12.002560. PubMed
1265 PMID: 20125830.
1266 77. Schnapf JL, Kraft TW, Nunn BJ, Baylor DA. Spectral sensitivity of primate photoreceptors.
1267 Vis Neurosci. 1988;1(3):255-61. Epub 1988/01/01. PubMed PMID: 3154798.
1268 78. Snodderly DM, Auran JD, Delori FC. The macular pigment. II. Spatial distribution in
1269 primate retinas. Invest Ophthalmol Vis Sci. 1984;25(6):674-85. Epub 1984/06/01. PubMed PMID:
1270 6724837.
1271 79. Snodderly DM, Brown PK, Delori FC, Auran JD. The macular pigment. I. Absorbance
1272 spectra, localization, and discrimination from other yellow pigments in primate retinas. Invest
1273 Ophthalmol Vis Sci. 1984;25(6):660-73. Epub 1984/06/01. PubMed PMID: 6724836.
1274 80. Lamb TD. Photoreceptor spectral sensitivities: Common shape in the long-wavelength
1275 region. Vision Research. 1995;35(22):3083-91. doi: https://doi.org/10.1016/0042-
1276 6989(95)00114-F.
1277 81. Govardovskii VI, Fyhrquist N, Reuter TOM, Kuzmin DG, Donner K. In search of the visual
1278 pigment template. Visual Neuroscience. 2000;17(4):509-28. Epub 2000/07/01. doi:
1279 10.1017/S0952523800174036.
1280 82. Bowmaker JK. Cone Visual Pigments in Monkeys and Humans. Advances in
1281 Photoreception: Proceedings of a Symposium on Frontiers of Visual Science: National Academies
1282 Press; 1990.
1283 83. Boettner EA. Spectral Transmission of the Eye. The University of Michigan, Final Report,
1284 Air Force Contract F41(609)-2966. 1967.
1285 84. Dobkins KR, Thiele A, Albright TD. Comparison of red-green equiluminance points in
1286 humans and macaques: evidence for different L:M cone ratios between species. Journal of the
1287 Optical Society of America A, Optics, image science, and vision. 2000;17(3):545-56. Epub
1288 2000/03/09. PubMed PMID: 10708036.

85. Estevez O, Spekreijse H. The "silent substitution" method in visual research. Vision Res. 1982;22(6):681-91. Epub 1982/01/01. doi: 10.1016/0042-6989(82)90104-3. PubMed PMID: 7112962.
86. Brainard DH. The Psychophysics Toolbox. Spat Vis. 1997;10(4):433-6. Epub 1997/01/01. PubMed PMID: 9176952.
87. Passaglia CL, Troy JB, Rüttiger L, Lee BB. Orientation sensitivity of ganglion cells in primate retina. Vision Research. 2002;42(6):683-94. doi: https://doi.org/10.1016/S0042-6989(01)00312-1.
88. Yang Q, Zhang J, Nozato K, Saito K, Williams DR, Roorda A, et al. Closed-loop optical stabilization and digital image registration in adaptive optics scanning light ophthalmoscopy. Biomedical optics express. 2014;5(9):3174-91. Epub 2014/11/18. doi: 10.1364/boe.5.003174. PubMed PMID: 25401030; PubMed Central PMCID: PMCPMC4230869.
89. Ku HH. Notes on the use of propagation of error formulas. Journal of Research of the National Bureau of Standards. 1966;70(4):263-73.
90. Enroth-Cugell C, Robson JG. The contrast sensitivity of retinal ganglion cells of the cat. J Physiol. 1966;187(3):517-52. Epub 1966/12/01. doi: 10.1113/jphysiol.1966.sp008107. PubMed PMID: 16783910; PubMed Central PMCID: PMCPMC1395960.
91. Cottaris NP, Jiang H, Ding X, Wandell BA, Brainard DH. A computational-observer model of spatial contrast sensitivity: Effects of wave-front-based optics, cone-mosaic structure, and inference engine. Journal of Vision. 2019;19(4):8-. doi: 10.1167/19.4.8.
92. Cottaris NP, Wandell BA, Rieke F, Brainard DH. A computational observer model of spatial contrast sensitivity: Effects of photocurrent encoding, fixational eye movements, and inference engine. Journal of Vision. 2020;20(7):17-. doi: 10.1167/jov.20.7.17.
93. Stockman A, Sharpe LT, Fach C. The spectral sensitivity of the human short-wavelength sensitive cones derived from thresholds and color matches. Vision Res. 1999;39(17):2901-27. Epub 1999/09/24. doi: 10.1016/s0042-6989(98)00225-9. PubMed PMID: 10492818.
94. Stockman A, Sharpe LT. The spectral sensitivities of the middle- and long-wavelength-sensitive cones derived from measurements in observers of known genotype. Vision Research. 2000;40(13):1711-37. doi: https://doi.org/10.1016/S0042-6989(00)00021-3.
95. Pokorny J, Smith VC, Lutze M. Aging of the human lens. Applied optics. 1987;26(8):1437-40. doi: 10.1364/AO.26.001437.
96. Dalkara D, Kolstad KD, Caporale N, Visel M, Klimczak RR, Schaffer DV, et al. Inner limiting membrane barriers to AAV-mediated retinal transduction from the vitreous. Molecular therapy : the journal of the American Society of Gene Therapy. 2009;17(12):2096-102. Epub 2009/08/13. doi: 10.1038/mt.2009.181. PubMed PMID: 19672248; PubMed Central PMCID: PMCPMC2814392.
97. Helga Kolb EF, Ralph N. Webvision : the organization of the retina and visual system: [Bethesda, Md.] : National Library of Medicine : [National Center for Biotechnology Information], 2007.; 2007.
98. Croner LJ, Purpura K, Kaplan E. Response variability in retinal ganglion cells of primates. Proceedings of the National Academy of Sciences. 1993;90(17):8128-30. doi: 10.1073/pnas.90.17.8128.
99. Yan W, Peng Y-R, van Zyl T, Regev A, Shekhar K, Juric D, et al. Cell Atlas of The Human Fovea and Peripheral Retina. Scientific reports. 2020;10(1):9802. doi: 10.1038/s41598-020-66092-9.

100. Packer O, Hendrickson AE, Curcio CA. Photoreceptor topography of the retina in the adult pigtail macaque (Macaca nemestrina). Journal of Comparative Neurology. 1989;288(1):165-83. doi: https://doi.org/10.1002/cne.902880113.

101. Provis JM, Hendrickson AE. The Foveal Avascular Region of Developing Human Retina. Archives of Ophthalmology. 2008;126(4):507-11. doi: 10.1001/archopht.126.4.507.

102. Bumsted K, Hendrickson A. Distribution and development of short-wavelength cones differ between Macaca monkey and human fovea. J Comp Neurol. 1999;403(4):502-16. Epub 1999/01/15. PubMed PMID: 9888315.

103. Patterson SS, Neitz M, Neitz J. Reconciling Color Vision Models With Midget Ganglion Cell Receptive Fields. Front Neurosci. 2019;13:865. Epub 2019/09/03. doi: 10.3389/fnins.2019.00865. PubMed PMID: 31474825; PubMed Central PMCID: PMCPMC6707431.

104. Tailby C, Solomon SG, Lennie P. Functional Asymmetries in Visual Pathways Carrying S-Cone Signals in Macaque. The Journal of Neuroscience. 2008;28(15):4078-87. doi: 10.1523/jneurosci.5338-07.2008.

105. van der Schaaf A, van Hateren JH. Modelling the Power Spectra of Natural Images: Statistics and Information. Vision Research. 1996;36(17):2759-70. doi: https://doi.org/10.1016/0042-6989(96)00002-8.

106. Lee BB, Sun H. The chromatic input to cells of the magnocellular pathway of primates. Journal of vision. 2009;9(2):1-18. doi: 10.1167/9.2.15. PubMed PMID: 19271925.

107. Diller L, Packer OS, Verweij J, McMahon MJ, Williams DR, Dacey DM. L and M cone contributions to the midget and parasol ganglion cell receptive fields of macaque monkey retina. J Neurosci. 2004;24(5):1079-88. Epub 2004/02/06. doi: 10.1523/JNEUROSCI.3828-03.2004. PubMed PMID: 14762126; PubMed Central PMCID: PMCPMC6793593.

1360 **Supporting Information**

1361 **S1 Fig. Soma sizes of RGCs for animals M2 and M3 across chromatic functional groups.** Observer
1362 1 used the open source software GIMP to segment RGCs in fluorescence images from M2 (large
1363 FOV), M3 (large FOV) and M3 (small FOV). The ellipse tool was used to segment the rough
1364 boundary of individual RGCs. Observer 2 used the open source software ImageJ to segment the
1365 same RGCs in fluorescence images from M2 and M3 using a hand tracing tool to trace the
1366 observable edges of each cell's fluorescence. Under both methods, the area for each cell was
1367 computed in terms of pixels^2 and then converted to µm^2 using the following formula: $\frac{\mu m}{pixel} =$
1368 $291.2\ \frac{\mu m}{deg} * \frac{axial\ length}{24.2\ mm} * \frac{FOV\ width}{496\ pixels}$, where 291.2 µm/deg is the human model eye visual angle to
1369 retinal extent conversion, 24.2 mm is the human model eye axial length, 496 pixels is the width
1370 of the imaging PMT used in the AOSLO system, axial length is the animal's axial length in mm, and
1371 FOV width is the width in degrees of the FOV used. The axial length of animal M2 is 17.2 mm, and
1372 the FOV width used was 3.64 deg. The axial length of animal M3 is 16.56 mm, and the FOV widths
1373 used were 3.69 deg (large FOV) and 2.54 deg (small FOV). Cells were compared across functional
1374 groups identified as L-M/M-L chromatic opponent (L-M), S only responding (S), Luminance only
1375 or achromatic (LUM), and mixed L-M/S responses (L-M/S). In **(a)**, the soma areas in µm^2 for the
1376 four functional groups in M2 are listed as the mean and standard deviation of each group across
1377 both observers. In **(b)**, the same comparisons are made for the four functional groups in M3 at
1378 the large FOV. In **(c)**, comparisons for the two functional groups found in M3 at the inner edge of
1379 the foveal slope (small FOV) are made across both observers. In, **(d)**, summary tables show the p-
1380 scores from a Mann-Whitney U test (MATLAB function ranksum(x,y)) comparing the distributions
1381 of soma areas across functional groups as measured by both observers separately. All p-values
1382 were greater than 0.1, except for Observer 2's comparison of the L-M group to the S only group

in M2 which had p = 0.0118. Based on these results, we cannot reject the hypothesis that the distributions of soma sizes for these functional groups are roughly the same across the two animals measured at the range of eccentricities at which we imaged cell somas.

S2 Fig. Spatial response of RGCs from M3 in the large FOV condition. Some example responses of L-M/M-L chromatic opponent RGCs from M3 at the large FOV, where each plot is the response of a different cell to drifting gratings (6 Hz) of spatial frequencies from 2 – 34 c/deg. These cells were chosen to showcase different cell responses and are not necessarily special or representative of the population. Purple and Orange curves show two separate experiments that were averaged together (Gray curve). The Blue curves are simple difference of Gaussians fits (not the full ISETBio modeling, for reasons explained below) to each average. Each plot title includes the cell's unique label "cN", and five parameters—the center strength K_c, the center radius r_c, the surround strength K_s, the surround radius r_s, and a goodness of fit value for the difference of Gaussians. As can be easily seen, many of the cells do not exhibit high spatial frequency falloff at the range of spatial frequencies measured, and so the difference of Gaussians either fits poorly or produces fit parameters that are highly irregular or suspect such as center sizes much smaller than the size of a single cone. For this reason, these data were not incorporated into the modelling in the main body, as higher spatial frequency responses were needed to properly fit many of these cell responses. There were 48 such L-M/M-L chromatic opponent cells in the large FOV in M3 out of 145 measured cells. In M2, there was only one experiment measuring response to spatial frequency and it suffered from the same lack of high spatial frequency measurements as the data shown here. Full data from both animals can be shared upon request.

1406 **S3 Fig. Spatial response of achromatic RGCs from M3 at the center of the foveola.** Each graph
1407 represents a single cell identified as responding only to achromatic stimuli from the center of the
1408 foveola of M3. The measured responses were to drifting gratings (6 Hz) of spatial frequencies
1409 from 4 – 49 c/deg. Purple, Orange, and Green lines represent the cell's response in three different
1410 experiments. The Gray line is the average of the three experiments for each cell, and the Blue line
1411 is a simple difference of Gaussians fit to the average (not the full ISETBio model, see S2 Fig). Each
1412 plot title includes the cell's unique label "cN", and five parameters—the center strength K_c, the
1413 center radius r_c, the surround strength K_s, the surround radius r_s, and a goodness of fit value for
1414 the difference of Gaussians. Compared to the 15 L-M and M-L cone opponent cells from this same
1415 location, these 7 achromatic cells were had noisier responses across experiments and more varied
1416 response characteristics. Though most of these cells are likely to be parasol RGCs, some could be
1417 achromatic midget RGCs or other rarer achromatic RGC types. Due to this uncertainty, these data
1418 were not included in the modelling for putative midget RGCs presented in the main manuscript.
1419 There were also achromatic cells identified in M2 and in M3 at the large FOV condition, but those
1420 data suffer from decreased resolution and a decreased range of spatial frequencies presented to
1421 the cells. Full data from all animals can be shared upon request.
1422
1423 **S4 Fig. Cone mosaic modelling fits compared to data from M3.** Images showing the performance
1424 of the ISETBio cone mosaic generator compared to the actual data from M3. At top, the model
1425 trichromatic photoreceptor mosaic generated by ISETBio (left) and the corresponding model cone
1426 density (right) (compare to Fig. 1b). At bottom left, a comparison of the median diameter of cones
1427 are compared between the model and the M3 data. At bottom middle and bottom right, the cone
1428 diameters of the model and measured data from M3 are compared across the horizontal and
1429 vertical meridians respectively.

1430

1431 **S5 Fig. Model cross-validation**. RMS errors for the 4 modeling scenarios we considered are
1432 depicted for 12 cells. Yellow and blue bars indicate insample and out-of-sample performance,
1433 respectively. During in-sample performance assessment the model is trained and evaluated using
1434 data from the same recording session. During out-of-sample performance assessment, the model
1435 is trained in one session and evaluated using data from another session. The data do not have
1436 enough power to reveal a model with best generalizing (out-of-sample) performance. In a few
1437 cells, the 1-cone/0.00D residual defocus model can be ruled out as its performance is significantly
1438 worse than the remaining 3. A two sample t-test with unequal variance was used to test against
1439 the hypothesis that there is a significant difference in the mean RMS fit errors between 2 modeling
1440 scenarios.

1441

1442 **S6 Fig. Optimization of residual defocus for different RGCs.** For each cell the optimal residual
1443 defocus value for the single cone center and multi-cone center model scenarios was calculated to
1444 gauge variability from the chosen 0.067 D reported in the main text. For each cell, the RMSE is
1445 shown for various residual defocus values for both model scarios. Cells are labeled L1-11 or M1-4
1446 according to whether we believed they were likely to contain an L cone or M cone at their center.

1447

1448 **S7 Fig. All four model scenario fits for the 15 L-M and M-L cone opponent RGCs from the center
1449 of the fovea of M3.** Four model scenarios were considered for all 15 cells: single cone centers
1450 with 0 D residual defocus, single cone centers with 0.067 D residual defocus, multi-cone centers
1451 with 0 D residual defocus, and multi-cone centers with 0.067 D residual defocus. As can be seen
1452 from the fits, the single cone center with 0.067 D defocus performs well for all 15 cells and
1453 produces center-surround structures that are consistent with what has been measured from

physiology. Cells are labeled L1-11 or M1-4 according to whether we believed they were likely to contain an L cone or M cone at their center.

S8 Fig. Simple center-surround model estimating percentage of achromatic midget RGCs. A simple model cone mosaic using hexagonal packing was created in MATLAB for the centermost 2400 cones (radius of 25 cones from the foveal center). Each cone was randomly assigned to be an L cone (48%), M cone (48%), or S cone (4%). For this simple model, a midget RGC was assumed to connect to one cone at its receptive field center and 6 cones at its surround (immediately adjacent to the center cone). For each model midget RGC, the proportion of cones that were the same type as the center cone was calculated. RGCs with all 6 surround cones of the same type as the center were classified as 'true achromatic' (orange histogram), and RGCs with at least 5 surround cones of the same type as the center were classified as 'thresholded achromatic' (blue histogram). The entire model simulation was then repeated 10,000 times, with a different randomly assigned cone mosaic each time. The histograms above show the number of simulations for which each percentage of midget RGCs that were either true achromatic or thresholded achromatic occurred. Based on this simple model, truly achromatic midget RGCs might make up approximately 1.5% of total midget RGCs at the foveal center, while thresholded achromatic midget RGCs might make up approximately 9% of total midget RGCs at the foveal center.

Figure 1

Click here to access/download;Figure;Fig1.tif

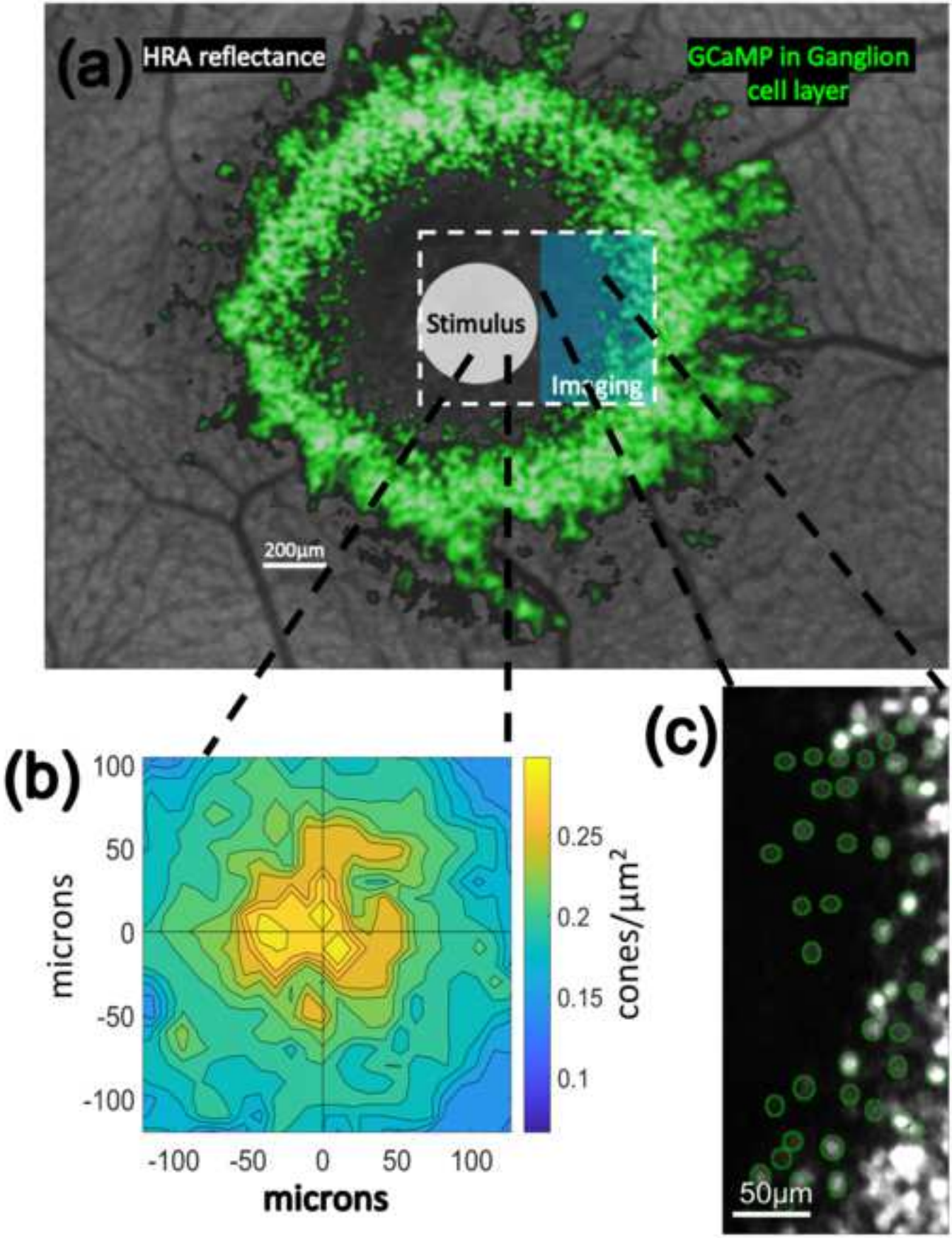

Figure 2

Click here to access/download;Figure;Fig2.tif

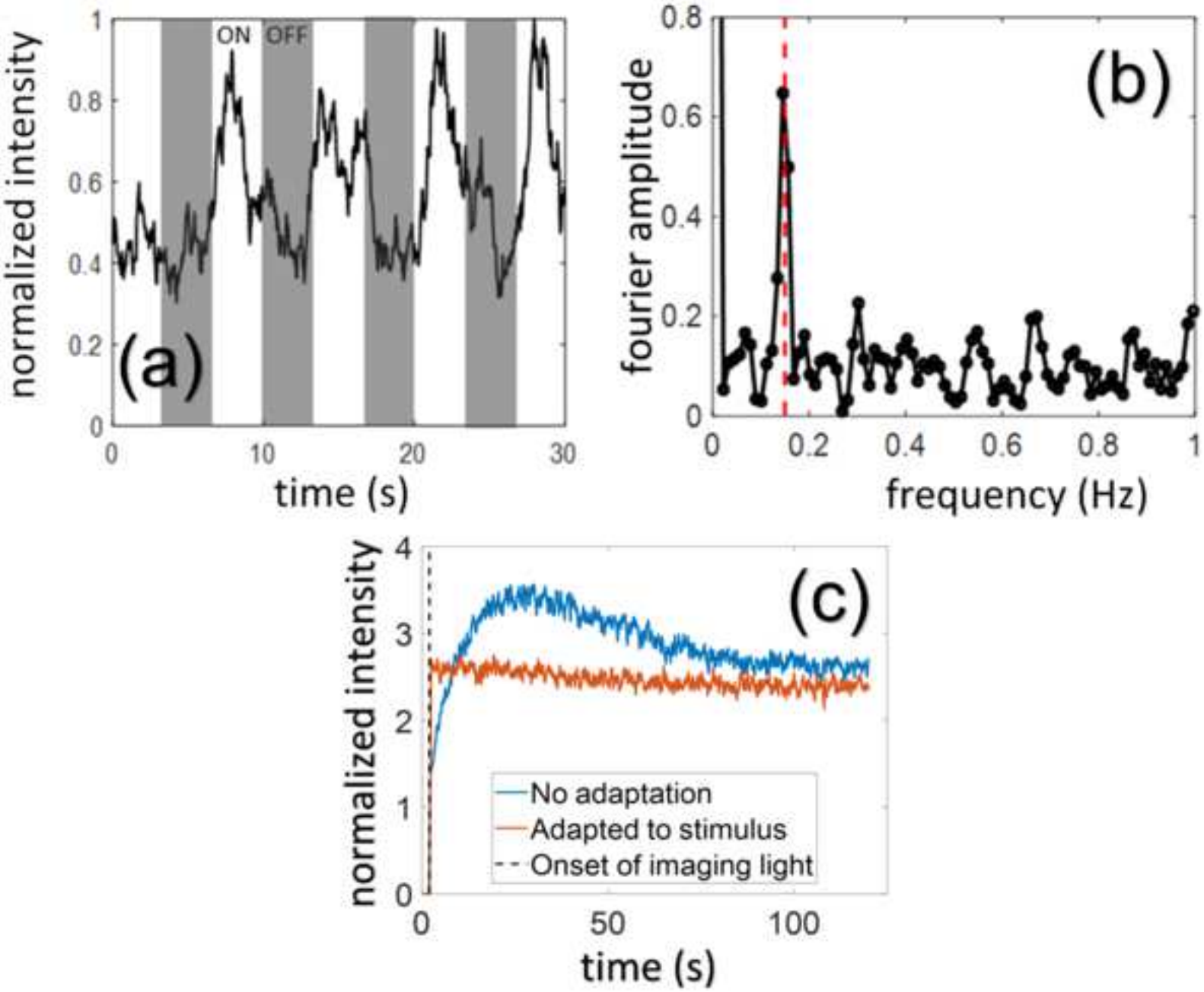

Figure 3

Click here to access/download;Figure;Fig3.tif

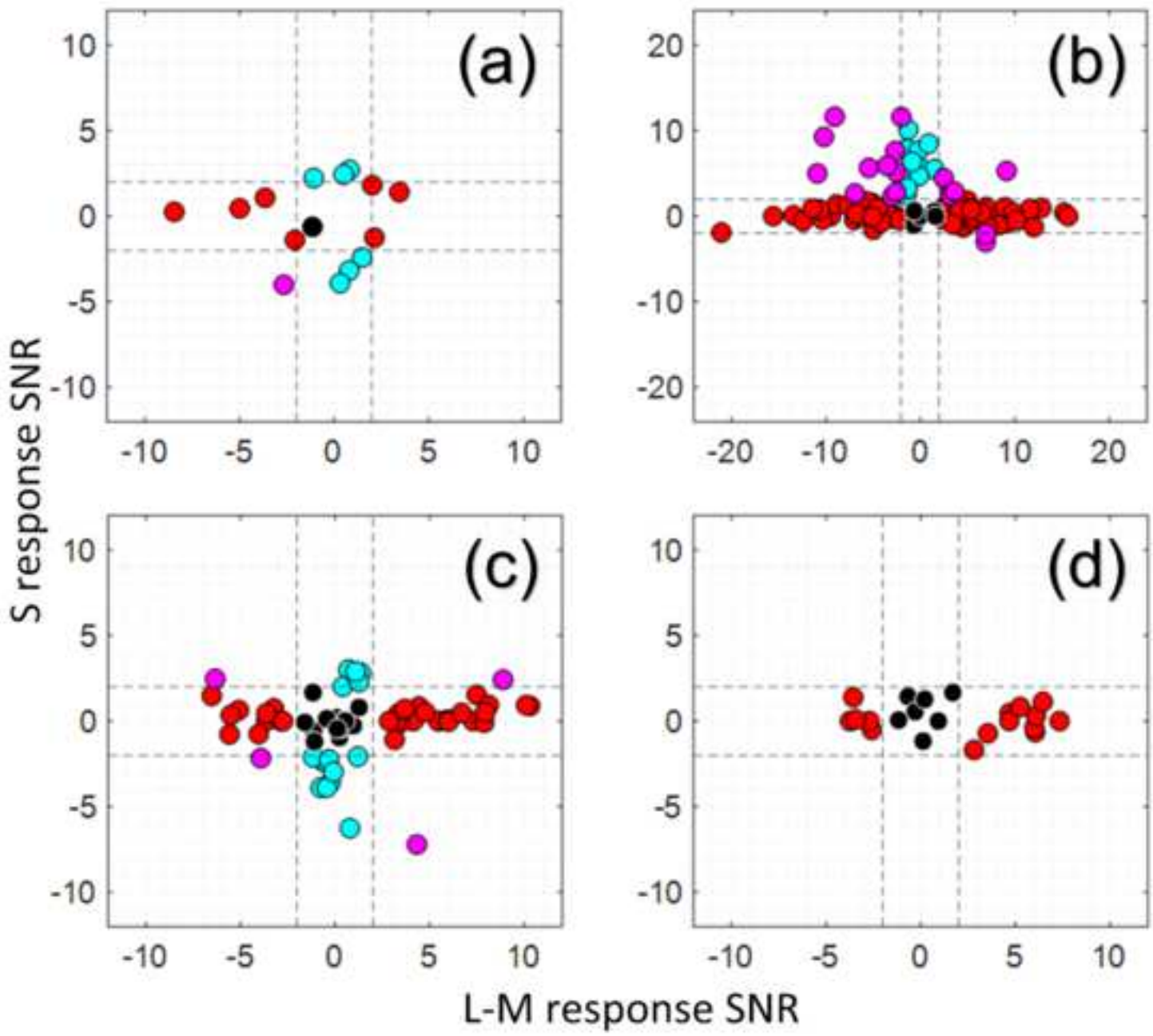

Figure 4

Click here to access/download;Figure;Fig4.tif

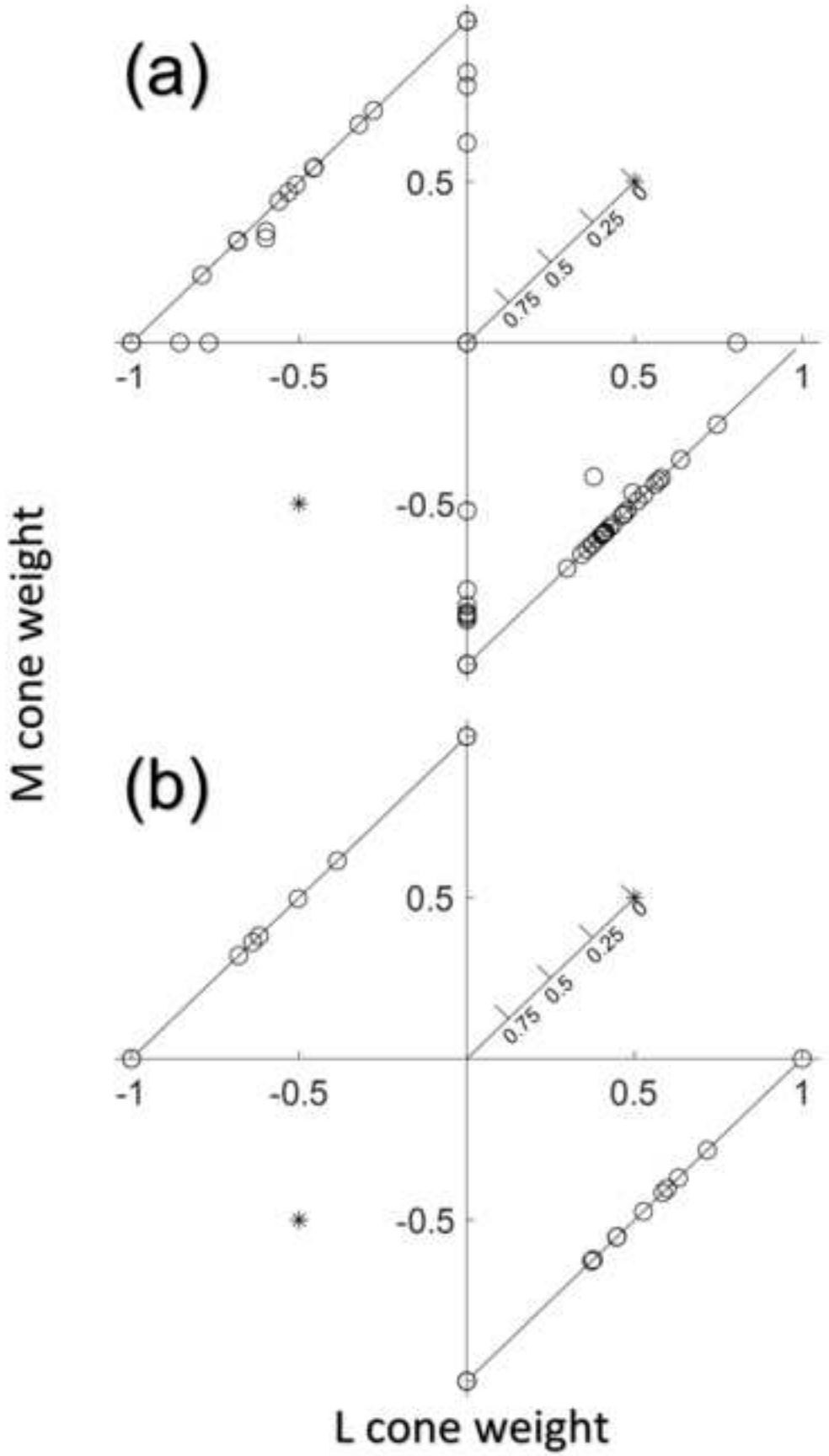

Figure 5

Click here to access/download;Figure;Fig5.tif

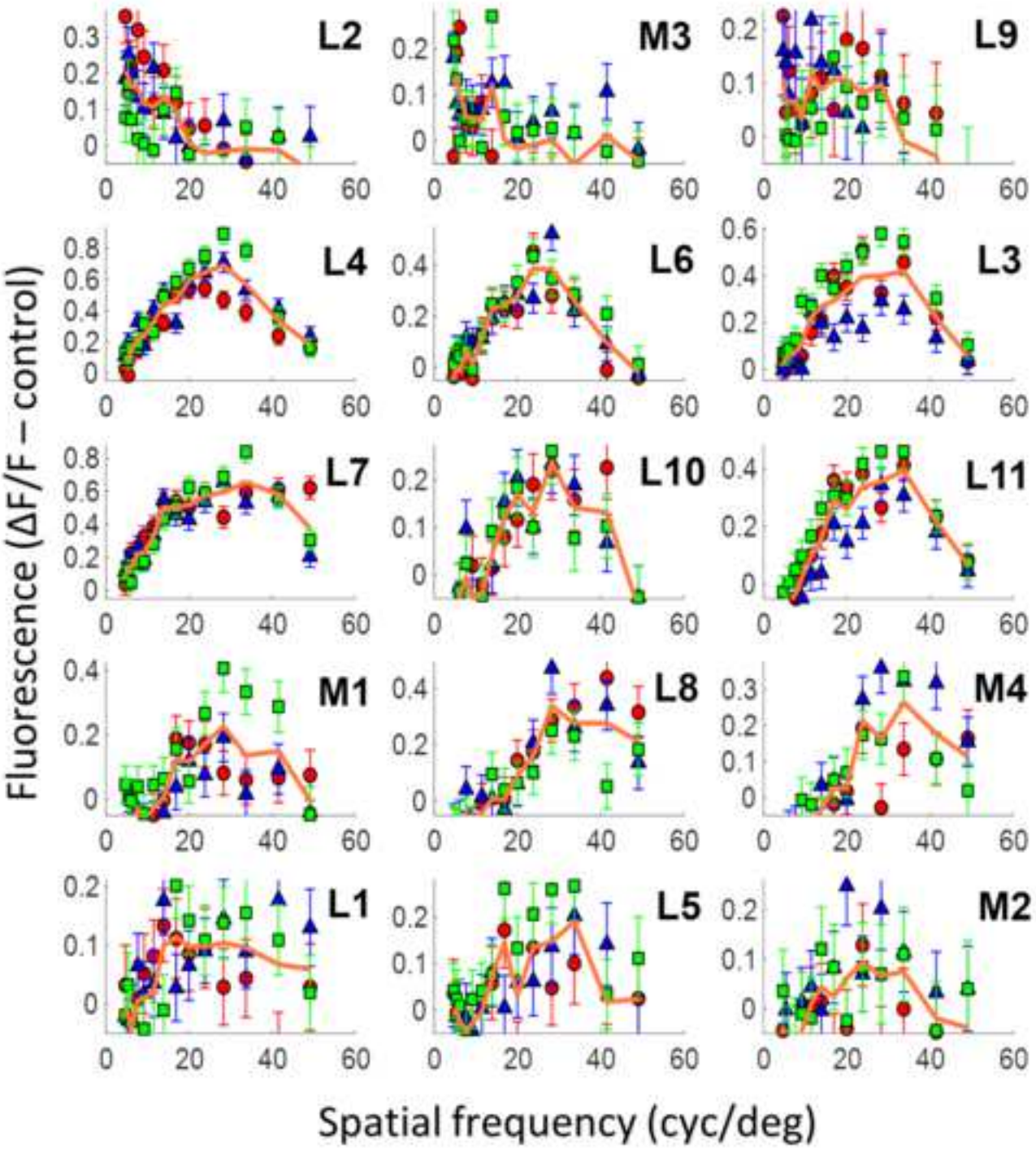

Figure 6

Click here to access/download;Figure;Fig6.tif

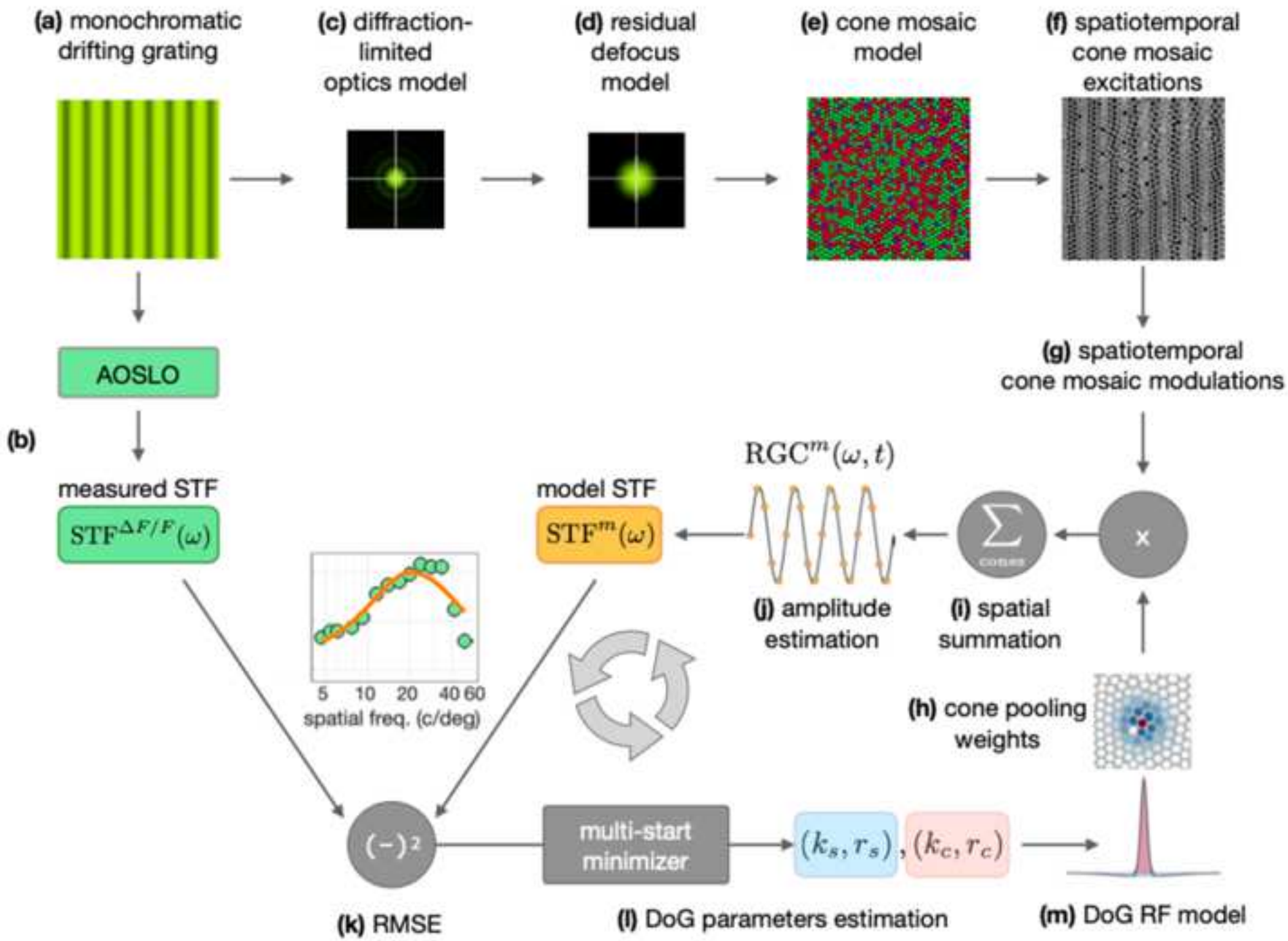

Figure 7

Click here to access/download;Figure;Fig7.tif

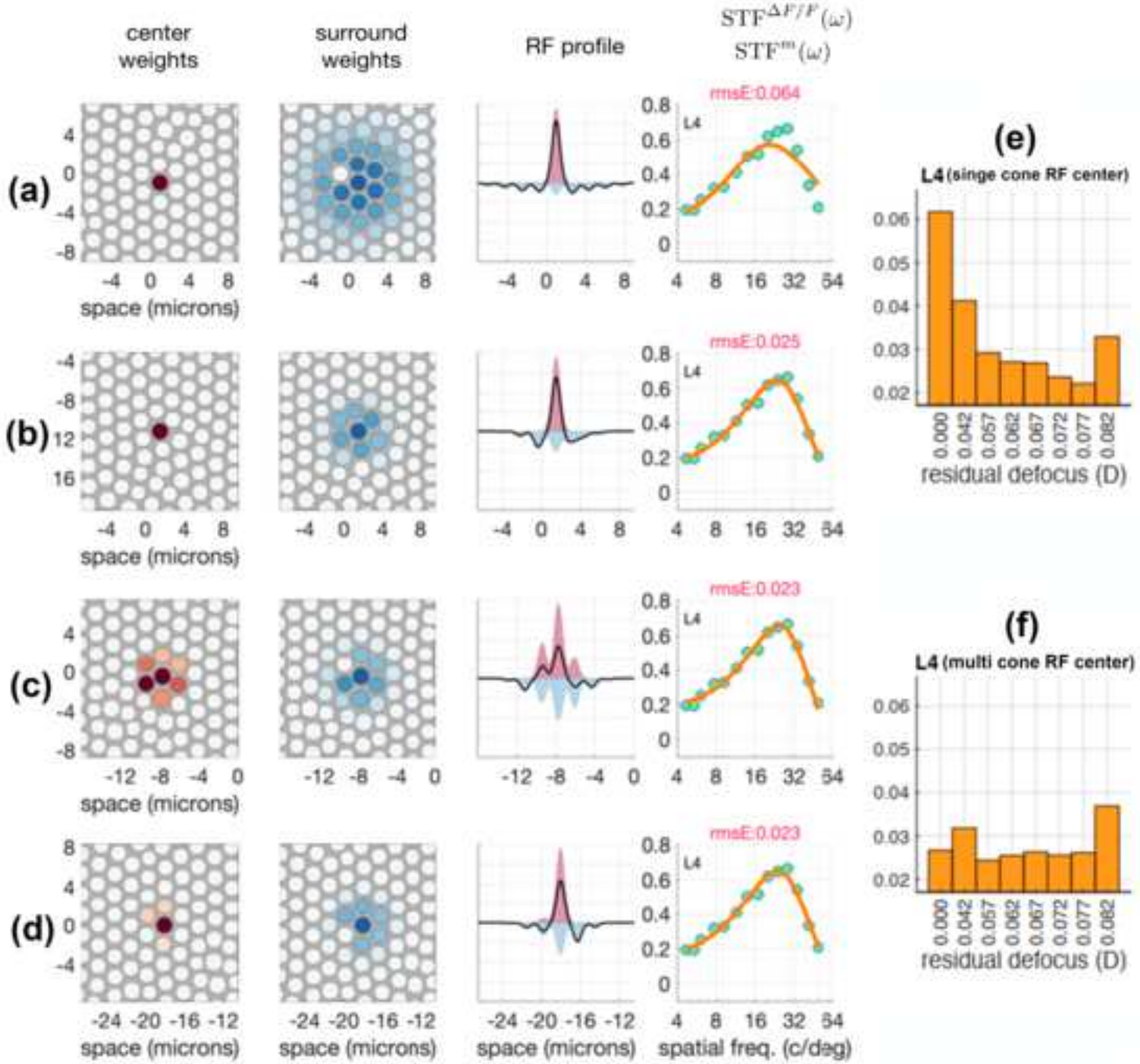

Figure 8

Click here to access/download;Figure;Fig8.tif

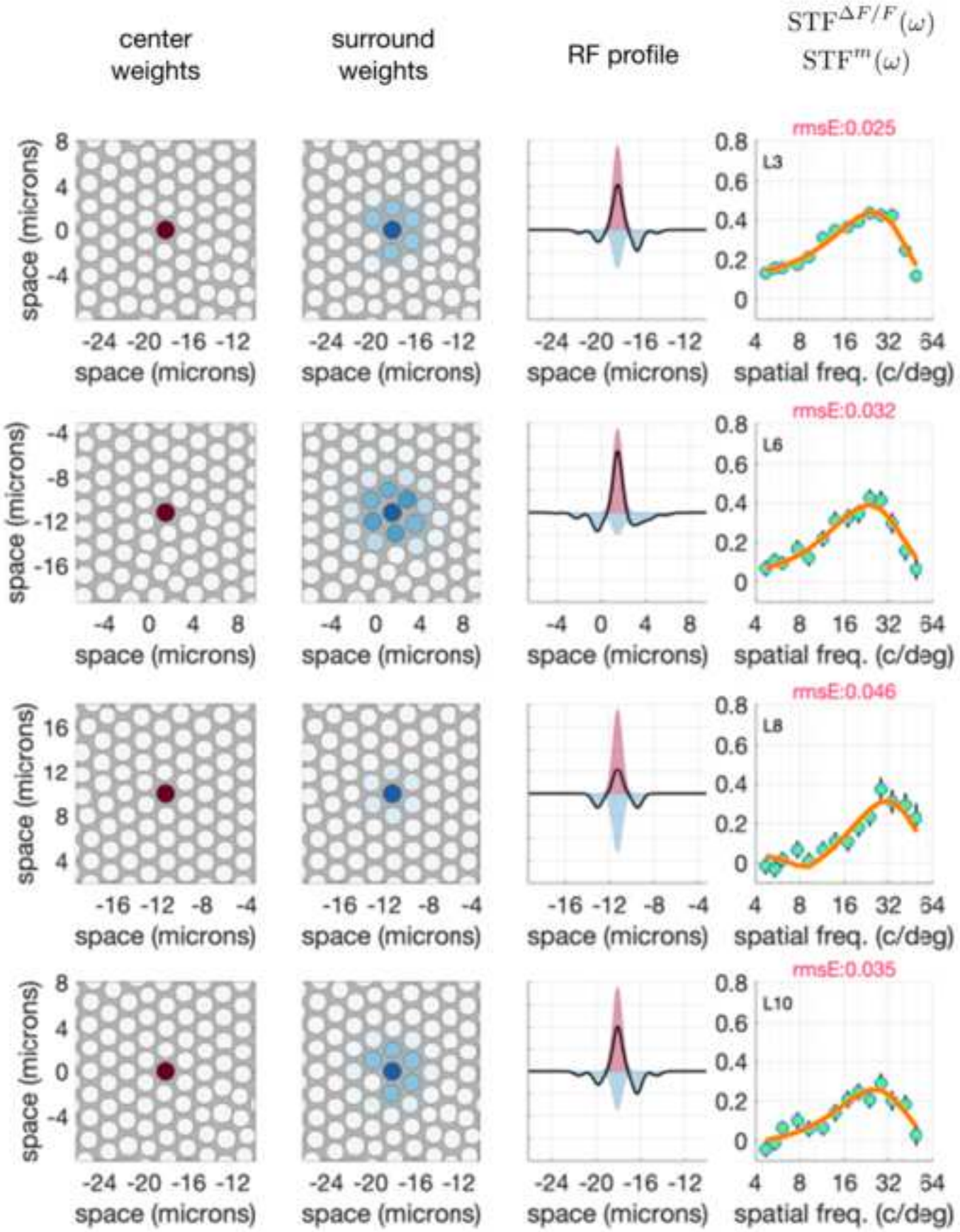

Figure 9

Click here to access/download;Figure;Fig9.tif

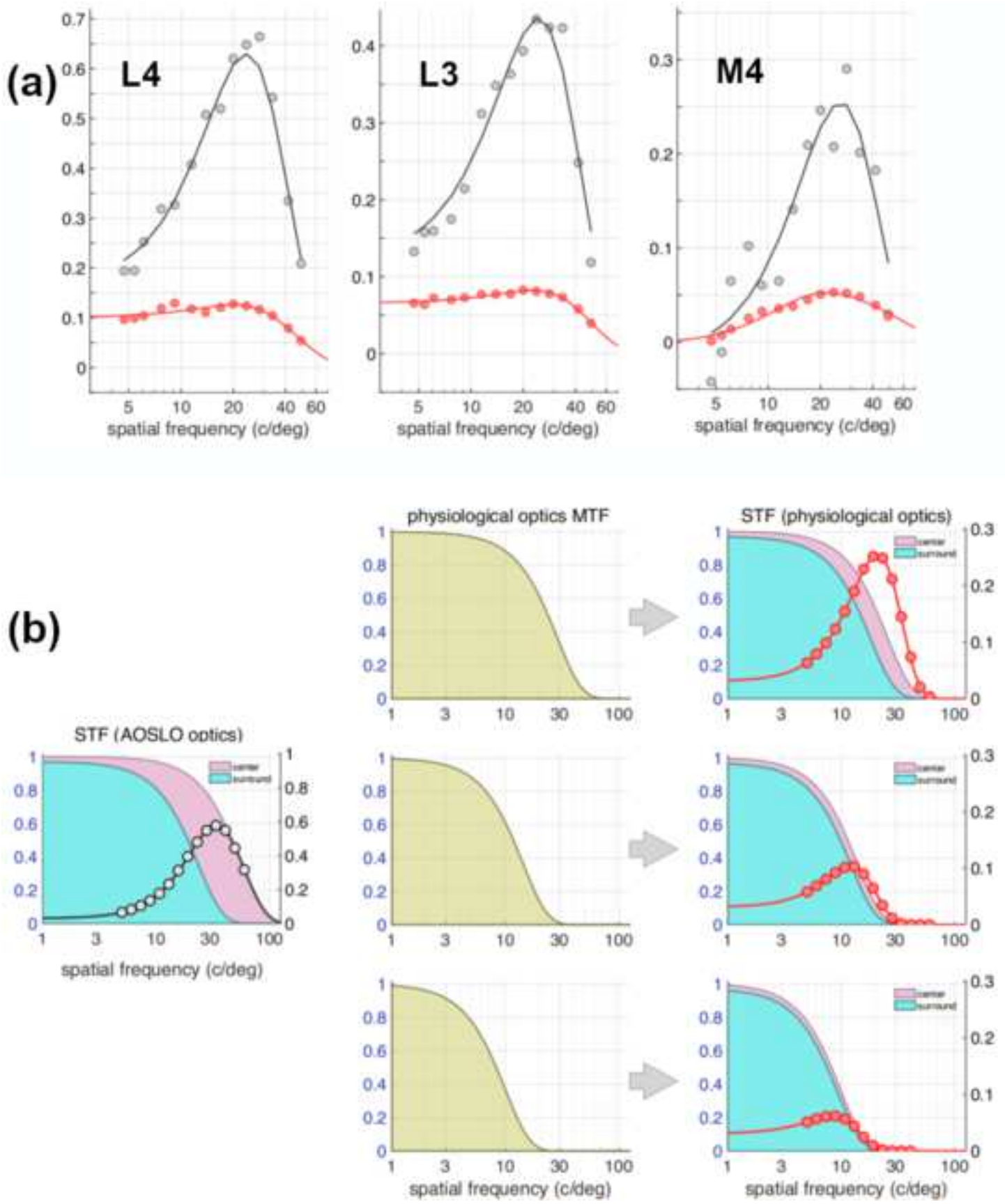

Figure 10

Click here to access/download;Figure;Fig10.tif

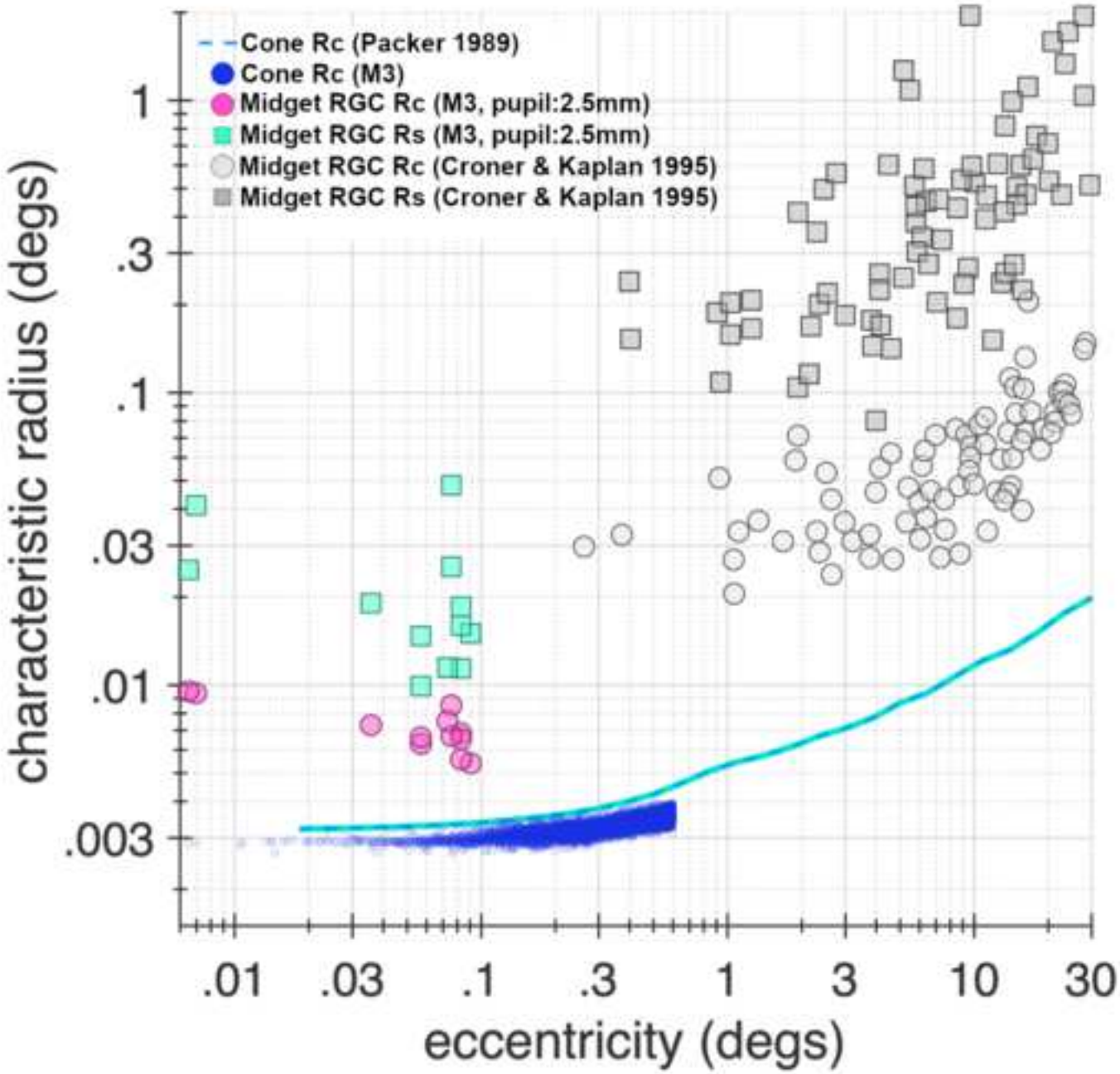

Figure 11

Click here to access/download;Figure;Fig11.tif

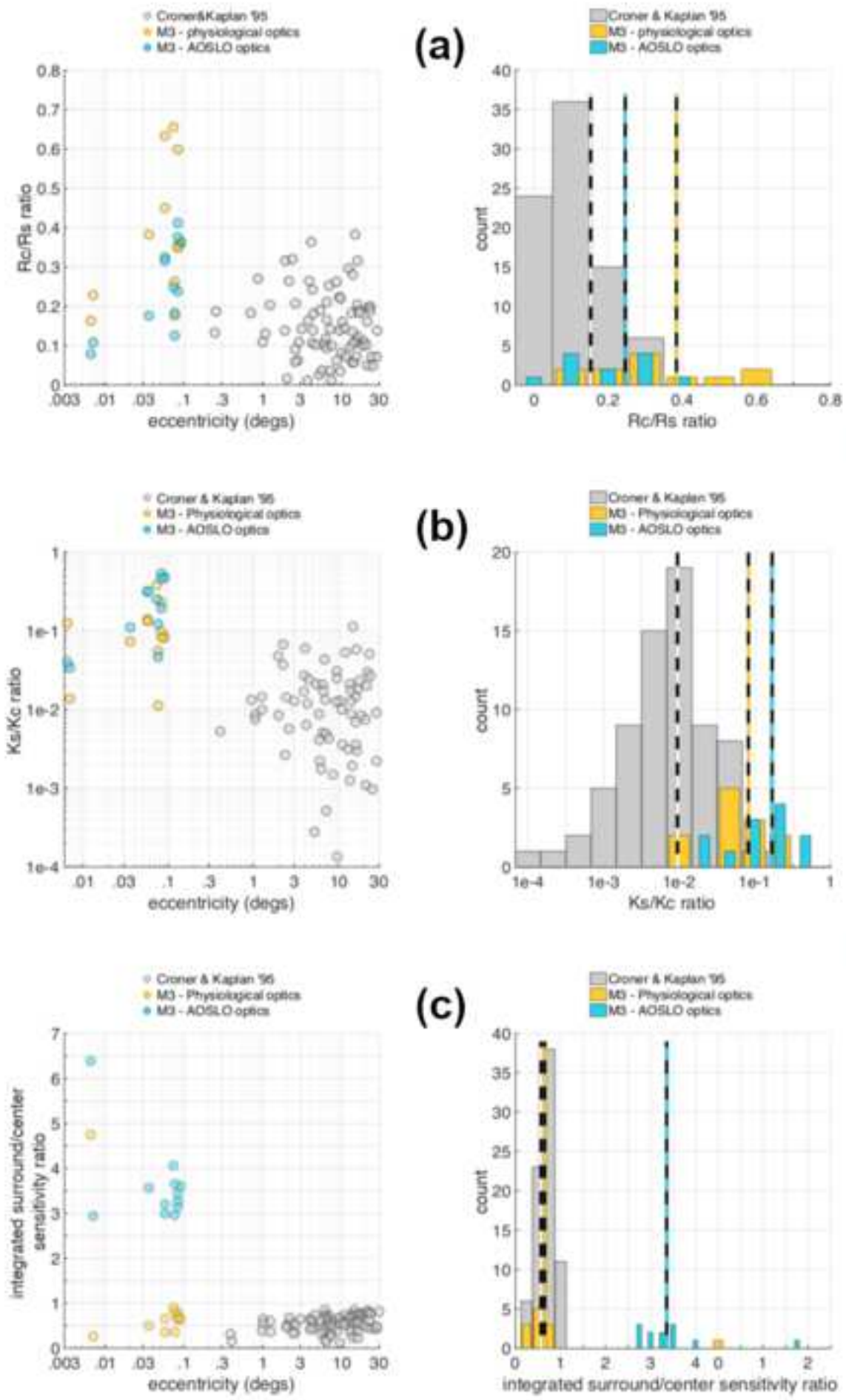

Click here to access/download
Supporting Information
S1_Fig.pdf

Click here to access/download
Supporting Information
S2_Fig.pdf

Click here to access/download
Supporting Information
S3_Fig.pdf

Click here to access/download
Supporting Information
S4_Fig.pdf

Click here to access/download
Supporting Information
S5_Fig.pdf

Click here to access/download
Supporting Information
S6_Fig.pdf

Click here to access/download
Supporting Information
S7_Fig.pdf

Click here to access/download
Supporting Information
S8_Fig.pdf